Electronic Supplementary Information (ESI)

Ni/Co/Ti layered double hydroxide for highly efficient photocatalytic degradation of Rhodamine B and Acid Red G: a comparative study

Priyadarshi Roy Chowdhury [a,*] and Krishna G. Bhattacharyya [a,*]

Corresponding authors' information
Department of Chemistry, Gauhati University, Guwahati-781014, Assam, India
***Tel**: +91 (0) 9435249993, +91 (0) 99864031987; **Fax**: +91 (0) 361 2570599*
***E-mail:** priyadarshiroychowdhury@yahoo.in; kgbhattacharyya@gmail.com*

Contents **Page Number**

S1. Structure of the test dyes

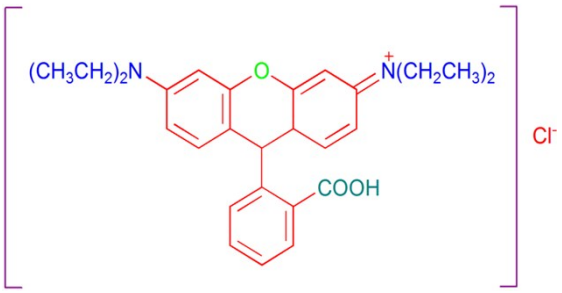

Fig. S1. Structure of Rhodamine B (RhB)

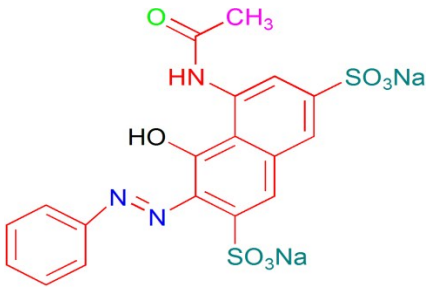

Fig. S2. Structure of Acid Red G (ARG)

S2. Scheme of Ni/Co/Ti LDH synthesis

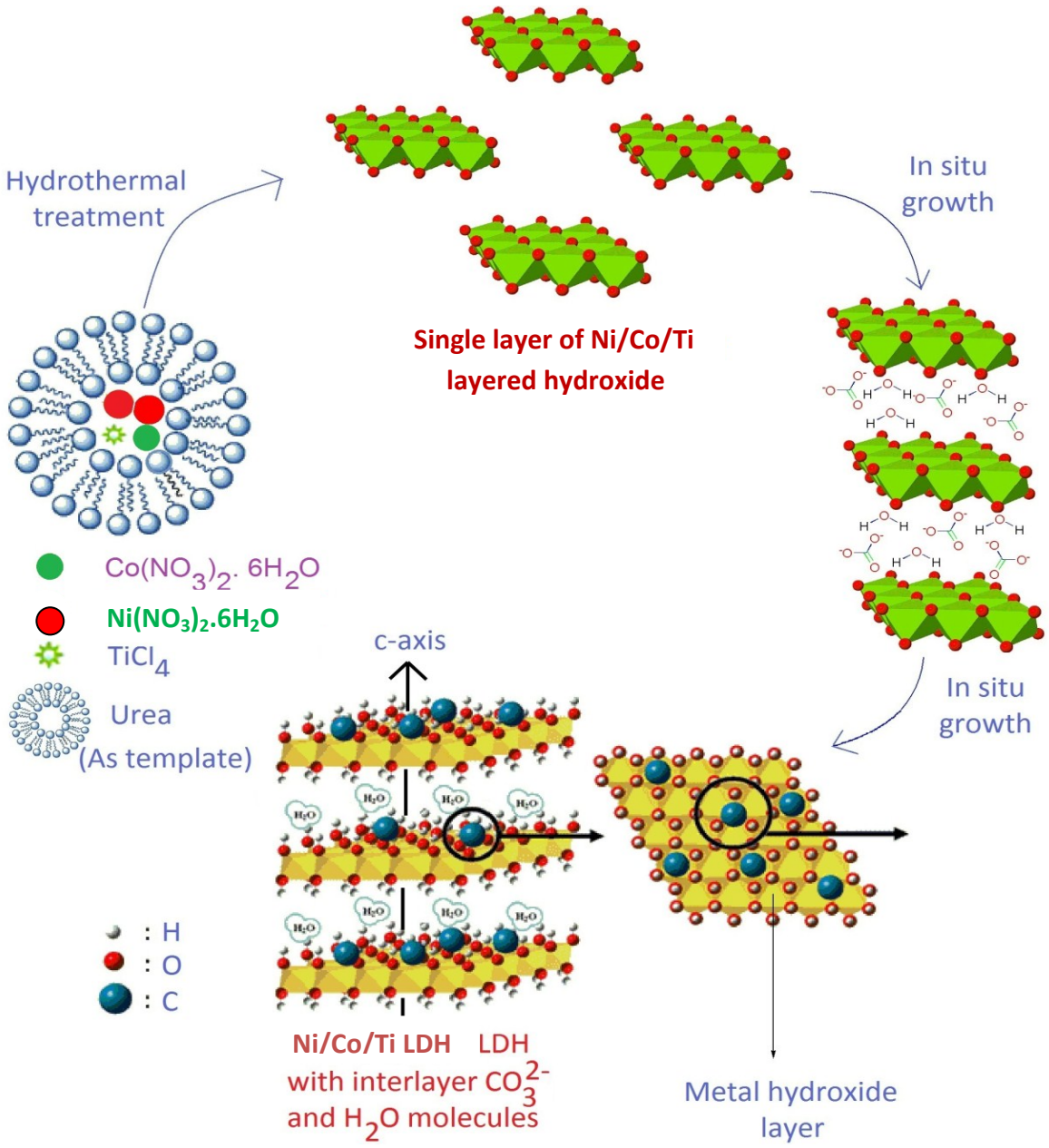

Fig. S3. Scheme of hydrothermal synthesis of 2:1:1 Ni/Co/Ti LDH with interlayer CO_3^{2-} and H_2O molecules

S3. Characterization techniques

Powder X-ray diffraction (XRD) pattern of the Ni/Co/Ti LDH was investigated using a PANalytical X'Pert PRO diffractometer using a monochromated CuK_{α} X-ray radiation source (λ= 1.5418 Å) at 25 mA and 35 kV at a scanning rate of 4 °min^{-1} and 2θ angle between 5° and 80°. The morphology, multilayered structure, lattice fringes of the sample were analysed by transmission electron microscopy (TEM) using a JEOL JEM-2010 TEM having an accelerating voltage of 200 kV, accompanied by an energy dispersive X-ray spectrometer (EDS) for analyzing the elemental composition. A Zeiss Supra 55 SEM instrument under 20 kV accelerating voltage was also used to investigate the morphology of the nanomaterial. The number of brucite layers of the LDH was calculated using a tapping mode atomic force microscopy (AFM; Cypher S Oxford instruments) having a Si tip of 10 nm radius (Mikronmasch), being used to achieve high resolution. 3D AFM micrograph was recorded simultaneously with 512 x 512 pixels with 1–2 Hz scan rate. The electrochemical impedance spectroscopy (EIS) analysis was performed on a CHI 760E electrochemical workstation using a three-electrode configuration: (i) Pt wire as the counter electrode (ii) a saturated calomel electrode (SCE) as a reference electrode and (iii) LDH deposited on ITO glass constituted the working electrode. The impedance measurements were performed using 0.5 M Na_2SO_4 solution as the electrolyte. Photoluminescence (PL) spectra at different excitation wavelengths were investigated using Hitachi F-2500 FL spectrophotometer comprising of a Xe lamp as excitation source. Time-resolved photoluminescence (TRPL) analysis was carried out measured at room temperature using a PicoQuant Fluo Time 300 lifetime spectrophotometer. X-ray photoelectron spectroscopy (XPS) was performed on PHI Quantum 5900 ESCA instrument in order to identify the chemical states and understand the nature of bonding taking place between the different groups present on the LDH surface. The LDH sample was irradiated with Al K_{α} X-rays at 1486.6 eV under ultrahigh vacuum conditions for XPS analysis. The UV–Visible diffuse reflectance spectroscopy of the LDH was studied on a Hitachi U4100 spectrometer, equipped with an integrating sphere attachment and using $BaSO_4$ background. The specific surface area and pore size distribution of the LDH was investigated by low temperature multipoint N_2-sorption-desorption measurements following Brunauer–Emmett–Teller (BET) method using a Micromeritics Tristar 3000 V6.08 analyzer. Prior to the analysis, the LDH was degassed at 120 °C under a vacuum condition for 3 h to remove the moisture

content. The LDH was subjected to dynamic light scattering (DLS) at different pH values by using a Malvern Zetasizer Nano ZS instrument to determine the variation of electrostatic surface charge with pH. Fourier transform infrared spectra (FT-IR) analysis was performed using a Shimadzu FT-IR 3000 spectrometer in the wavenumber range of 400–4000 cm^{-1}. The LDH sample was mixed with KBr in 1:100 weight ratio of sample to KBr and compressed into pellets for analysis. The thermal stability of the LDH was investigated by thermogravimetric analysis (TG) in N_2 atmosphere from 32 °C to 750 °C with a heating rate of 10 °C/min, using a Mettler Toledo thermal analyser. The presence of hydroxyl radical ($^{\bullet}OH$), generated from the LDH during photoassisted degradations was measured using a terephthalic acid (TA) fluorescence probe. The superoxide radicals $(O_2^{\bullet -})$ generated on the LDH during photocatalysis was investigated by electron paramagnetic resonance (EPR) spectroscopy, recorded using a Bruker EMX X-band spectrometer with a field modulation of 100 kHz. The absorbance of the reaction mixtures of the photocatalytic experiments were investigated using a Shimadzu 1800 UV-visible spectrometer. The colourless breakdown products of the photoassisted degradations were identified using a Varian 3900 GC-Saturn 2100T GC-MS, having column temperature of 45 °C (1 min) and 45–250 °C (5 °C/min, hold time: 5 min). The complete mineralization of the metabolites of the dyes were analysed by measuring the Total Organic Carbon (TOC) using a ANATOC II, TOC analyser. In order to determine the carbon mass balance associated with degradation, arrangements were made to connect the reactor with the GC, ion chromatograph and a TOC analyser.

S4. X-ray diffraction analysis

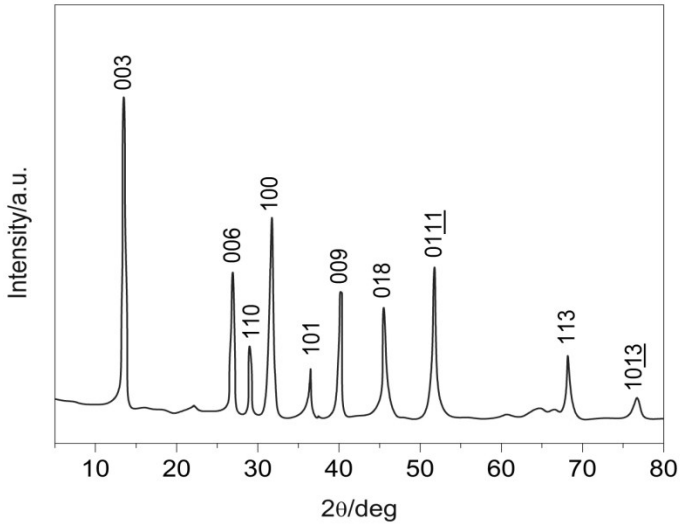

Fig. S4. X-ray diffractogram of 2:1:1 Ni/Co/Ti LDH

Table S1: X-ray diffraction parameters of 2:1:1 Ni/Co/Ti LDH

h	k	l	2θ/deg	FWHM/deg	d-spacing/nm	Relative intensity
0	0	3	13.42	0.825	0.664	73.21
0	0	6	26.56	0.236	0.334	46.48
0	0	9	41.05	0.242	0.225	33.65
1	1	0	28.56	0.216	0.313	29.34
1	0	0	32.48	0.427	0.271	55.28
1	0	1	37.43	0.329	0.263	26.58
0	1	8	45.28	0.232	0.217	32.43
1	1	$\underline{11}$	53.05	0.218	0.186	42.56
1	1	3	67.47	0.825	0.145	24.46
1	0	$\underline{13}$	76.35	0.912	0.132	14.25

Table S2: Lattice parameters of 2:1:1 Ni/Co/Ti LDH

Lattice parameters	2:1:1 Ni/Co/Ti LDH
Lattice parameter a	0.626 nm
Lattice parameter c	2.01 nm
Lattice parameter c′ (distance between the two consecutive brucite layers)	0.671 nm
Interlayer thickness[a]	0.289 nm
(003/006) peak height ratio	1.58

The X-ray diffraction pattern of the LDH could be indexed to a typical hexagonal lattice. The lattice parameter ‘c’ depends on anion size, hydratation and amount of interlayer anions, the parameter ‘a’ depends primarily on the cation–cation distance within the

layered framework. The cell parameters ‘a’ and ‘c’ are calculated using the following relations-

$a=2d_{110}$, c [$= (3d_{003}+6d_{006}+9d_{009})/3$] and $c=3c'$.[1]

Interlayer thickness= (c' — brucite-like sheet thickness); $c'= 0.671$ and

Brucite sheet thickness= 0.382 nm (calculated using cross-sectional HR-TEM and AFM analyses).

S5. SEM- EDX results

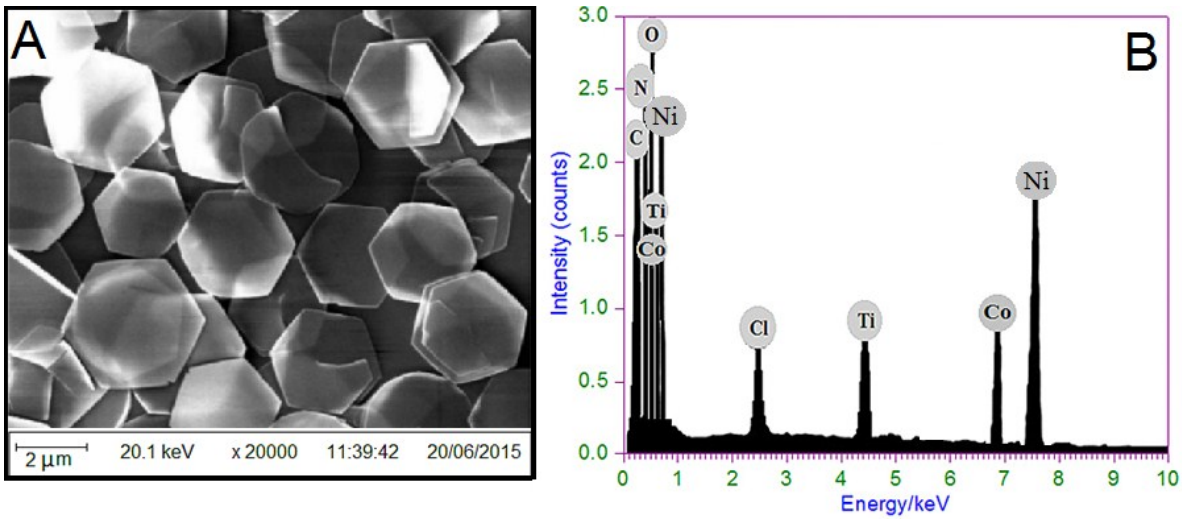

Fig. S5: (A) SEM image and (B) EDX spectra of 2:1:1 Ni/Co/Ti LDH

i) SEM analysis

The morphology of the 2:1:1 Ni/Co/Ti LDH nanomaterial investigated by SEM **[Fig. S5(A); ESI†]** revealed hexagonal shaped house-of-cards-type stacking of sheet-like crystallites, in good agreement with that of the HR-TEM observations. The existence of hexagonal platelets could be due to the subsequent crystallization of Ni/Co/Ti LDH nanoparticles favoured by hydrothermal conditions in basic medium.[2, 3,4]

ii) EDX analysis

The EDX analysis investigated the elemental composition of the 2:1:1 Ni/Co/Ti LDH **[Fig. S5(B); ESI†].** The EDX analysis showed good agreement between the atomic/weight ratio and the stoichiometric molar ratio of Ni, Co and Ti present within the LDH and the data is presented in **Table S3 (ESI†).** The existence of Cl in the EDX analysis (also observed in the XPS) is due use of $TiCl_4$ as the precursor of Ti during the LDH synthesis.

Table S3. Elemental composition revealed by EDX analysis for 2:1:1 Ni/Co/Ti LDH

Element	Weight %	Atomic %	Ni/Co/Ti (ratio)
C K	2.08	1.59	
N K	2.2	1.78	
O K	9.35	2.46	
Cl K	3.82	1.31	
Ni K	41.38	46.54	2.03:1.02:1
Co K	20.81	23.39	
Ti K	20.36	22.93	
Total	**100**	**100**	

S6. AFM images

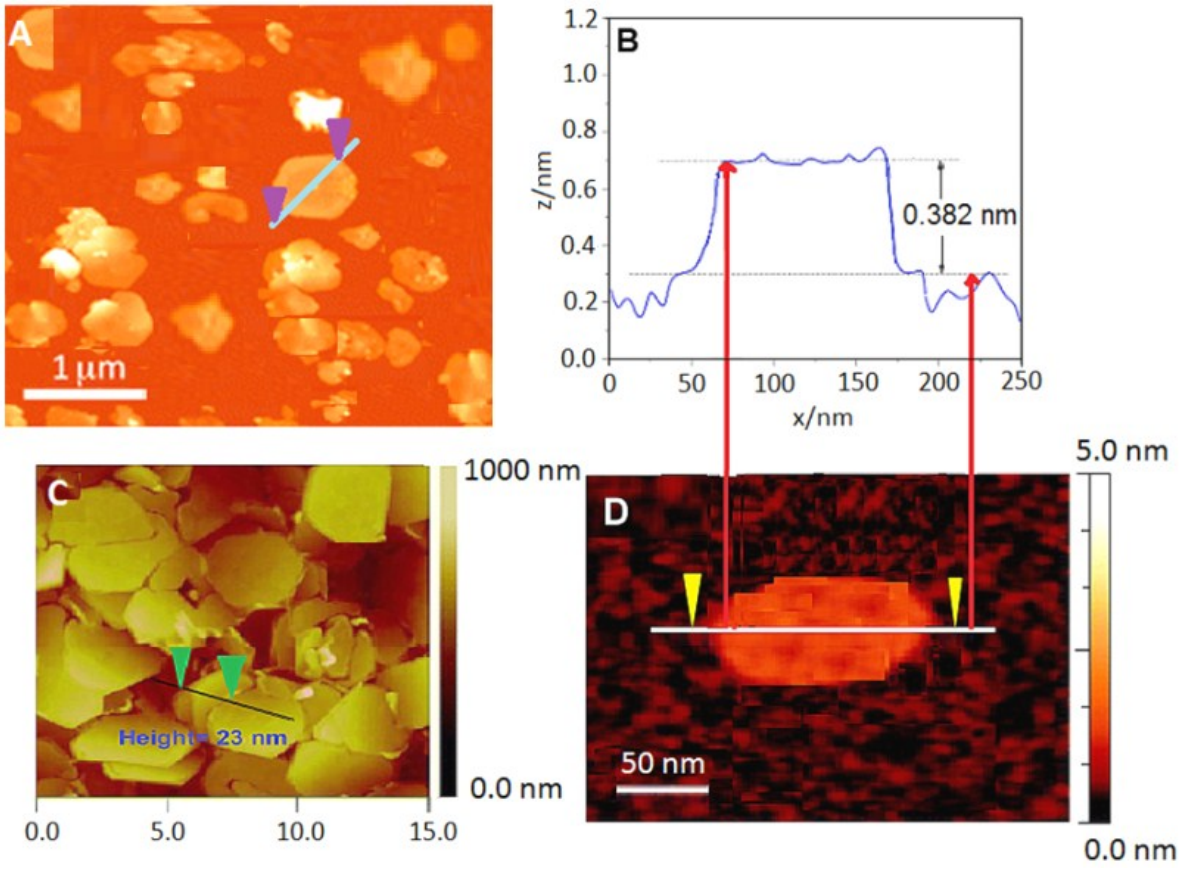

Fig. S6. (A) AFM image (B) Height profile of single crystallite (C) AFM image showing the total height (D) AFM image of single crystallite of 2:1:1 Ni/Co/Ti LDH

S7. XPS surface survey analysis

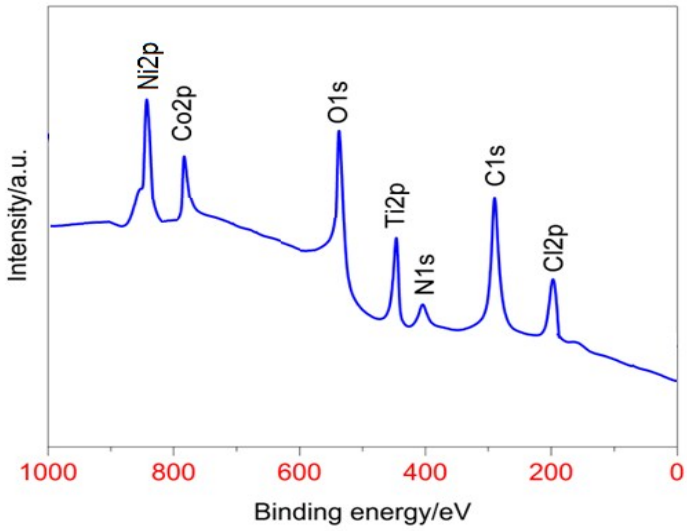

Fig. S7. XPS full scan survey spectrum of 2:1:1 Ni/Co/Ti LDH

The XPS full scan surface survey was performed using an Al K_α X-ray source to provide an insight into the surface states of the synthesized Ni/Co/Ti LDH nanomaterial. The existence of different chemical states of elements were identified by comparison of the obtained photoelectron binding energies (BE) with those taken from literature. It indicated the existence of spin states like Cl2p, C1s, N1s, Ti2p, O1s, Co2p and Ni2p respectively on the surface of the synthesized LDH. The X-ray photoelectron lines were further deconvoluted to investigate the existence of mixed valence states and nature of bonding of different groups on the LDH surface.[2,4] The full scan XPS survey spectrum is represented in **Fig. S7 (ESI†).**

The Ni $2p_{3/2}$ regions for the LDH showed the existence of peaks **[Fig. S8(A); ESI†]** in the range of 842 – 878 eV. A hump is observed at ~ 845 eV, that could be attributed to the LL_3VV Auger electron line of Ni. The asymmetric peak at 854.2 eV is attributed to the $2p_{3/2}$ spin state of Ni. The second peak at 872 eV is attributed to $2p_{1/2}$ spin state of Ni. Meanwhile, the other two peaks at ca. 863 eV and 875 eV could be assigned to their corresponding shake-up satellite lines. The XPS peaks were further confirmed by deconvolution, which showed the presence of these peaks and shake-up satellites at their respective positions.

The Co2p core level XPS lines yielded four peaks associated with $2p_{3/2}$ and $2p_{1/2}$ spin states of Co along with its corresponding satellite lines. These XPS lines were confirmed

further by deconvolution of Co2p line, which indicated two sharp peaks at 781 eV and 796 eV respectively corresponding to the $2p_{3/2}$ and $2p_{1/2}$ spin states of Co, with a peak splitting of 15 eV (=ΔE), representing the Co^{2+} and Co^{3+} states of Co. **[Fig. S8(B); ESI†].** Moreover, the deconvoluted low intensity XPS lines of 787 eV and 803 eV represented the satellite features of $2p_{3/2}$ and $2p_{1/2}$ spin states respectively.

The Ti2p XPS line **[Fig. S8(C); ESI†]** showed the existence of two asymmetric peaks at binding energies of 456.8 eV and 462.5 eV corresponding to $2p_{3/2}$ and $Ti2p_{1/2}$ spin states of Ti. Hence, the LDH surface is most likely to contain two spin states Ti with a peak separation of ~5.7 eV, indicating the existence of Ti^{4+} species, which was also confirmed from its XRD observations. The deconvoluted $Ti2p_{3/2}$ state indicated two peaks at 456.5 eV and 457.2 eV, thereby showing the existence of Ti^{3+} and Ti^{4+} respectively. The surface transformation of Ti-species also indicated the occurrence of redox reaction at the surface of the LDH. [3, 4]

The O1s XPS core level spectrum of the Ni/Co/Ti LDH nanomaterial reveals a peak at 529.9 eV, accompanied by a valley extending upto 536 eV. The deconvolution of O1s XPS line revealed the existence of eight XPS peaks **[Fig. S8 (D); ESI†]**. The deconvoluted O1s XPS signals at 529.7 eV and 529.9 eV corresponds to Ti_2O_3 and TiO_2 species present on the LDH surface. Meanwhile the O1s XPS lines at 530.2 eV could be attributed to NiO whereas that observed at 530.7 eV and 531 eV could be attributed to CoO and Co_2O_3 species respectively. The deconvoluted O1s line corresponding to 531.3 eV is most likely to be associated with the physisorbed H_2O or -OH groups present on the surface of the LDH. Meanwhile, the deconvoluted O1s XPS line at 532 eV could be indexed to C=O group of the interlayer CO_3^{2-} species. The low intensity deconvoluted signal of 535.2 eV could be due to the presence of NO_3^- species, which has occurred due to the use of nitrate salts of Ni and Co during the hydrothermal synthesis of LDH.

The C1s XPS line **[Fig. S8 (E); ESI†]** reveals a peak at 288 eV and its corresponding satellite feature is detected at 289.4 eV. The deconvoluted C1s lines appeared at binding energy positions of 288.1 eV and 289.5 eV, that could be attributed to C=O and O=C-O bonding of the interlayer CO_3^{2-} species present in the 2:1:1 Ni/Co/Ti LDH nanomaterial.

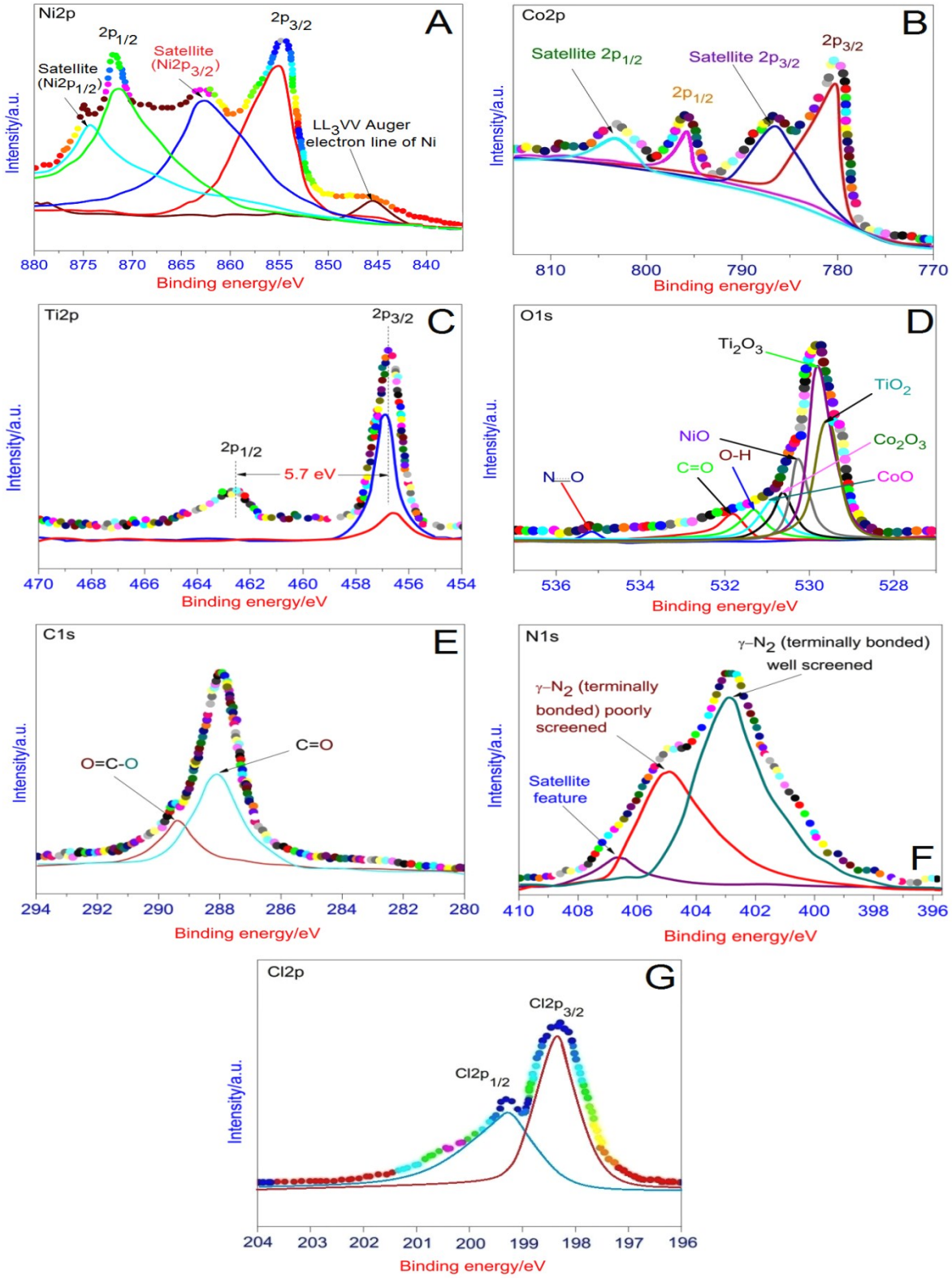

Fig. S8. XPS lines of (A) Ni2p (B) Co2p (C) Ti2p (D) O1s (E) C1s (F) N1s (G) Cl2p of Ni/Co/Ti LDH. HR-XPS lines are represented by color mapping and its deconvoluted are represented by solid lines. Deconvolution was performed with CASA XPS software (version 2.3.15)

The N1s core level line is considered to be highly sensitive to the chemical environment of the nitrogen species and varies between 396 to 410 eV **[Fig. S8 (F); ESI†]**. The peak at BE of 402.9 eV associated with its satellite feature at 405 eV extending upto 409 eV could be due to N_2 species present in the LDH surface. Deconvoluted N1s line yields three peaks at BE values of 402.8 eV, 405 eV and 406.8 eV respectively. The peaks at BE of 402.8 eV and 405 eV is attributed to well screened and poorly screened terminally bonded γ-N_2 species respectively. The low intensity deconvoluted peak at 406.8 eV could be assigned to its corresponding satellite feature. The observation of N1s XPS features is most likely due to the use of water soluble metal nitrate salts and urea (as a basic precipitant) in the synthesis of the LDH.

The XPS of Cl2p indicates two peaks corresponding the existence of $2p_{3/2}$ and $2p_{1/2}$ spin states at respective binding energies of 198.3 eV and 199.4 eV respectively **[Fig. S8 (G); ESI†]**. The occurrence of the deconvoluted peak at BE of 198.3 eV confirms the presence of $Cl2p_{3/2}$ state and that of 199.4 eV is due to $2p_{1/2}$ spin state of Cl. This indicates that Cl^- is physisorbed on the LDH surface. The origin of Cl2p core level XPS lines in the LDH is due to the use of $TiCl_4$ as a precursor of Ti during the LDH synthesis.[4]

S8. N_2 sorption isotherm and and pore size distribution and electrochemical impedance curves

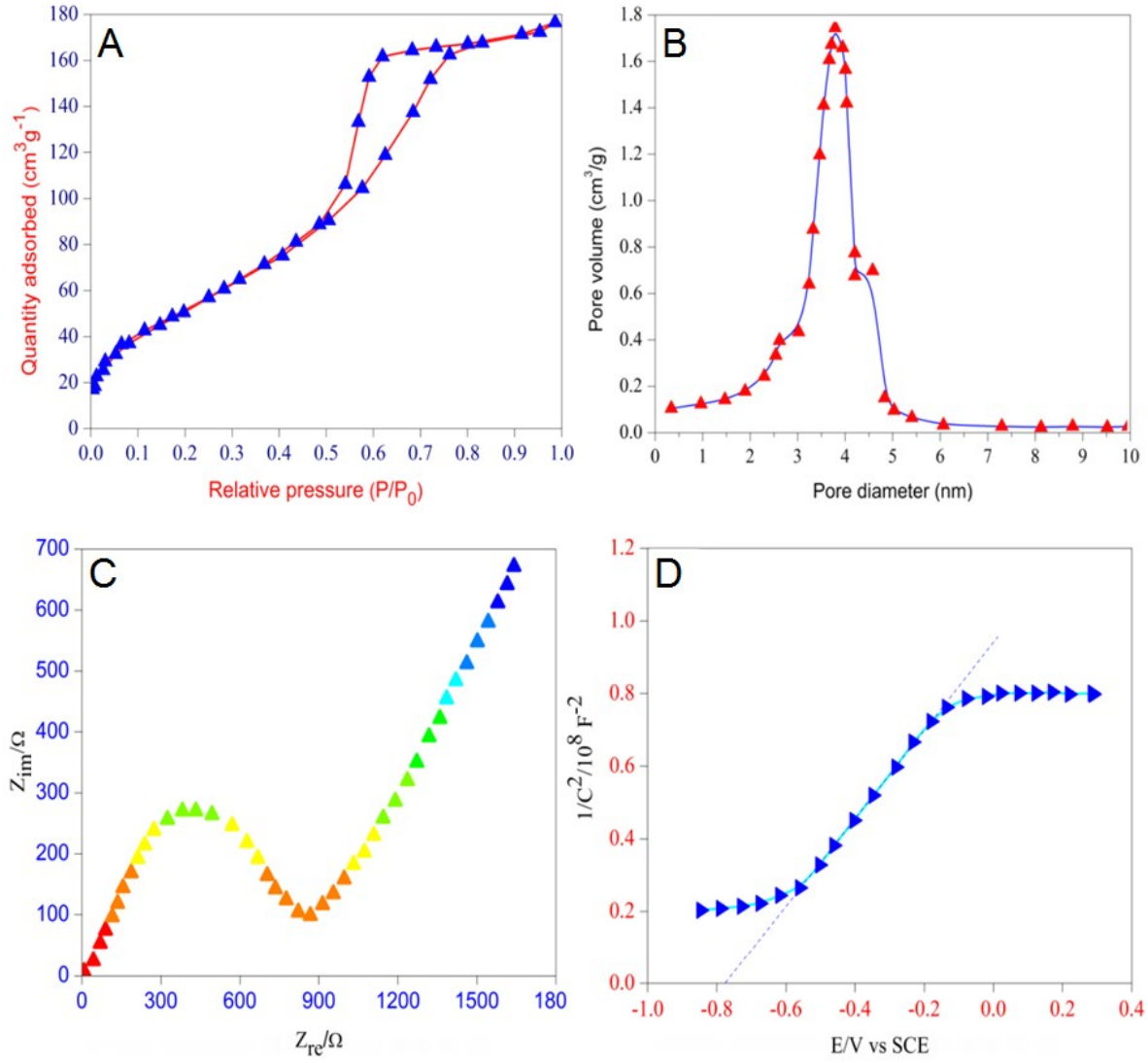

Fig. S9 (A) N_2-sorption desorption isotherm (B) Pore size distribution curve (C) Electrochemical Impedance Nyquist plot (D) Mott-Schottky impedance plot of 2:1:1 Ni/Co/Ti LDH

S9. TG and FT-IR curves

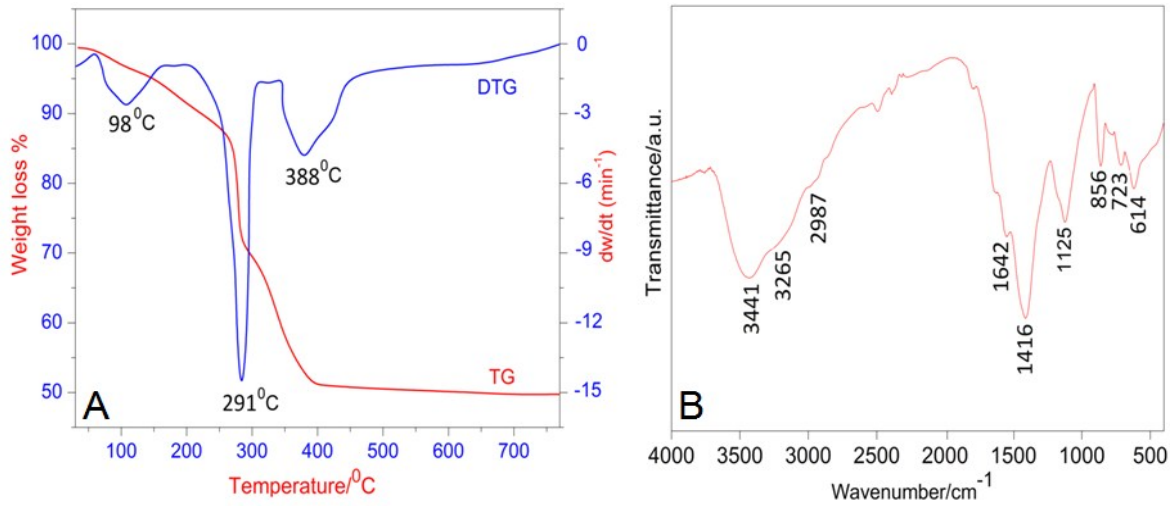

Fig. S10 (A) TG curve and (B) FT-IR spectrum of 2:1:1 Ni/Co/Ti LDH

i) FT-IR analysis

The FT-IR spectrum exhibited the characteristic frequencies associated with the CO_3^{2-} containing LDHs and the characteristic bands are presented in **Fig. S10 (B); (ESI†).** The absorption at 3441 cm^{-1} has been attributed to the stretching vibrations associated with the surface and interlayer H_2O molecules and OH^- groups, being observed at lower frequency position in the Mn/Co/Ti LDH, than that of free water at 3600 cm^{-1}, indicating clearly that H_2O has been present in the interlayer positions. The shoulders at 3265 cm^{-1} and 2987 cm^{-1} could be indexed to the H-bonding arising between the interlayer H_2O and CO_3^{2-} anions. The band at 1642 cm^{-1} has been assigned to the bending vibration of H_2O molecules.[3] In LDHs, three IR active vibrations arise from the interlayer CO_3^{2-} species particularly at 1416 cm^{-1} (υ_3), 1125 cm^{-1} (υ_1) and 723 cm^{-1} (υ_2). The bands 856 cm^{-1} and 614 cm^{-1} could be indexed to the M–OH and M–O bonds present in the LDH. The band at 856 cm^{-1} could also be attributed to the in-plane quadrant bending vibrations. The FT-IR peak at 1125 cm^{-1} is attributed to the C-O stretching vibrations. The 723 cm^{-1} IR vibration has been attributed the υ_2 mode of the interlayer CO_3^{2-} species. Thus, the presence of these bands, accompanied by the XRD and XPS results, confirms the presence of CO_3^{2-} ions and H_2O molecules in the interlayer galleries.[5-9]

S10. Photoluminescence analysis

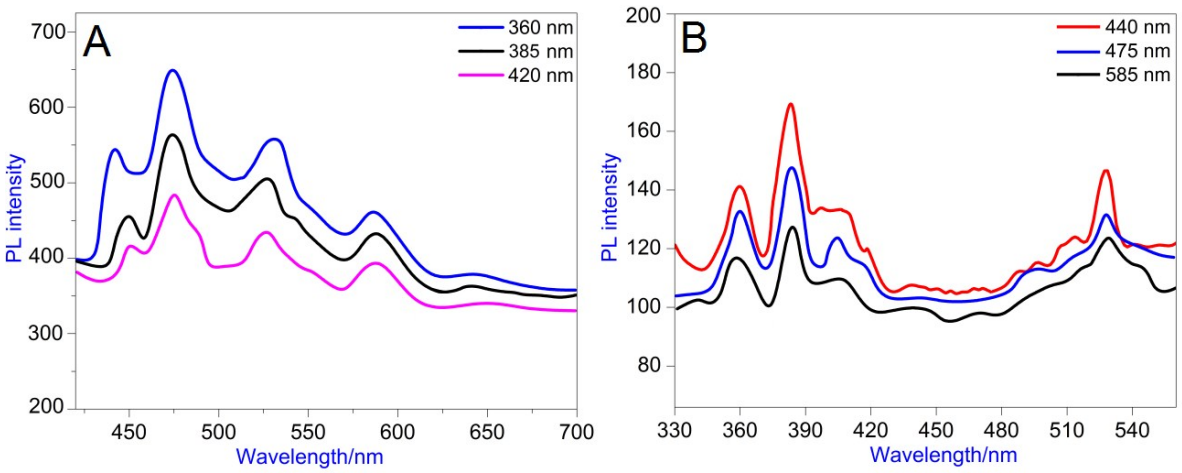

Fig. S11. (A) Emission spectra at different excitation wavelengths (B) Excitation spectra at different emission wavelengths of 2:1:1 Ni/Co/Ti LDH

i) Photoluminescence emission spectra analysis

The effects of recombination of photo-induced charge carriers on degradation was understood by photoluminescence (PL) analysis, carried out at room temperature. The PL emissions of semiconductors have been broadly classified into two categories: band–band PL emission belonging to the electronic transitions from the conduction band (CB) bottom to the valence band (VB) top and excitonic PL emissions that results from the surface oxygen vacancies and defects states of the semiconductors. In case of band–band PL emission, lower the PL intensity, higher is the separation rate of photo-induced electron (e_{CB}^-) - hole (h_{VB}^+) pair and hence a higher photocatalytic activity is being observed. However, a complicated relationship exists for the excitonic PL emissions, between PL intensity and photocatalytic activity; which primarily depends on the electronic properties of semiconductors. Herein, the emission analysis of Ni/Co/Ti LDH nanomaterial was carried out under excitation wavelengths corresponding to 360 nm, 385 nm and 420 nm respectively **[Fig. S11(A); ESI†]**. The PL intensity decreased on increasing the excitation wavelength, which could be attributed to the higher separation of the charge carriers, also consistent with the electrochemical impedance results. The oxygen vacancies and defects binds the photo-induced electrons to form excitons, so that the PL signal can occur easily. Studies have validated that Ti doped photocatalytic systems consist of two kinds of trap sites for holes- the deep hole and the shallow hole. The deep trapped holes show a lower

oxidizing potential and prefers mostly to undergo reaction with physisorbed substances. The synthesized LDH showed several excitonic PL emissions at 440 nm (2.80 eV), 475 nm (2.60 eV), 530 (2.33 eV) and 585 nm (2.11 eV) accompanied by a valley extending upto 675 nm respectively, resulting from the surface oxygen vacancies and defects present within the Ni/Co/Ti LDH, that has lead to a significant enhancement in its optical properties. The UV emission peak at 475 nm (2.60 eV) could be attributed to the exciton emission from conduction band (e_{CB}^-) to valence band (h_{VB}^+), which is in accordance with the band gap energy of the synthesized LDH (as determined from the Tauc plot analysis). The other emissions are mostly associated with excitons and oxygen defects related shallow as well as deep trap centers. The emission at 440 nm is due to the self-trapped exciton (STE). The STE is generated on the lattice site on a hole capture by a trapped electron. There are two types of STE- direct or indirect. A direct STE occurs due to direct recombination of the charge carriers, while in indirect STE emission the recombination occurs via an oxygen vacancies. Since Ti doping generates oxygen vacancy, the STE emission at 440 nm might be occurring via oxygen vacancies and is of indirect nature. The emission peaks at 475 nm is due to F-centers present within the LDH. The F center is the oxygen vacancy with two trapped electrons. These emissions associated with the oxygen defects occur as a result of the presence of oxygen vacancies in the shallow and deep levels within the band gap of the synthesized LDH. The oxygen defects present at the grain boundaries are distributed randomly; charged and acts as shallow trap levels. The luminescence peaks corresponding to 440 nm, 530 nm and 585 nm are associated with the shallow trap levels. The shoulders at ~630 nm extending upto 700 nm could be assigned to the emissions from the deep trap levels. The free electrons remaining untrapped by the defect sites are likely to migrate throughout the lattice and undergo recombination with the holes within or on the LDH surface. However, the migrating electrons are likely to be repelled by the charged oxygen vacancies preventing further recombination with the holes. As the defect states arise as a result of doping, the mobility of carriers is slowed down, which delays the recombination process. Apart from this, dopants present on the LDH surface also stand as an obstacle for efficient overlap of carriers on the LDH surface. The d-states act as active trap centers and separate the charge carriers. Doping shifts the band edges and hence, the conduction band electrons have to travel an indirect path for

undergoing recombination with the holes, which delays the recombination and quenches the emission intensity. Since the emission intensity is reduced on increasing the excitation wavelength, quenching effect is expected to play an important part in the reduction of the emission intensity. In conformity to this effect, doping of ions also increase the interaction between the dopant and defects thereby forming quenching centers. The electrons are first captured by shallow trap levels and jump to the Ni, Co or Ti d-states, which further jumps from one d-state to the other and thus forms some quenching centers. The electrons, after passing through a channel of dopant and defects, ultimately find recombination center and emits light. This process increases the time period for the carriers to undergo recombination and therefore reduces the emission intensity.[5] Thus, the presence of defects within the microstructures of the synthesized Ni/Co/Ti LDH nanomaterial is assumed to play a major role in its photoassisted degradation of dyestuffs.

ii) Photoluminescence excitation spectra analysis

The photoluminescence spectra the LDH nanomaterial was also monitored at different emission wavelengths in order to identify the accurate excitation luminescence wavelengths and the results are illustrated in **[Fig. S11 (B); ESI†].** The luminescence spectra of the LDH showed strong excitation peaks at 360 nm, 380 nm, 420 nm and 530 nm on being excited at the emission wavelengths corresponding to 440 nm, 475 nm and 585 nm respectively. The results thus obtained indicates the validity of the excitation wavelengths used to determine the luminescence properties of the LDH.[6,7]

iii) Time resolved photoluminescence emission analysis

The dynamics of photo-generated charge carriers are evaluated by time-resolved photoluminescence emission spectroscopy (TRES), the instrumentation is based on a streak camera which enables the calculation of the temporal decay time.[6] The luminescence data was fitted on a two-exponential function equation-

$$I(t) = A_1 \exp\left(\frac{t}{\tau_1}\right) + A_2 \exp\left(\frac{t}{\tau_2}\right) \qquad (1)$$

where τ_1, τ_2 represents the decay times of the fast and slow components; A_1, A_2 are the corresponding the luminescence amplitudes. Meanwhile, τ_2 is associated with the indirect

formation of self-trapped excitons generated by trapped electrons and τ_1 is due to the direct formation of free electrons and holes. The results of TRES are presented in **Fig. S11(C); (ESI†)** and **Table S4 (ESI†)**. A comparatively longer luminescence decay time for the LDH corresponding to the excitation of 420 nm, could be attributed to the delay in radiative recombination process.[7] As a result of the longer charge carrier lifetimes, a higher photocatalytic properties are being observed for the LDH.

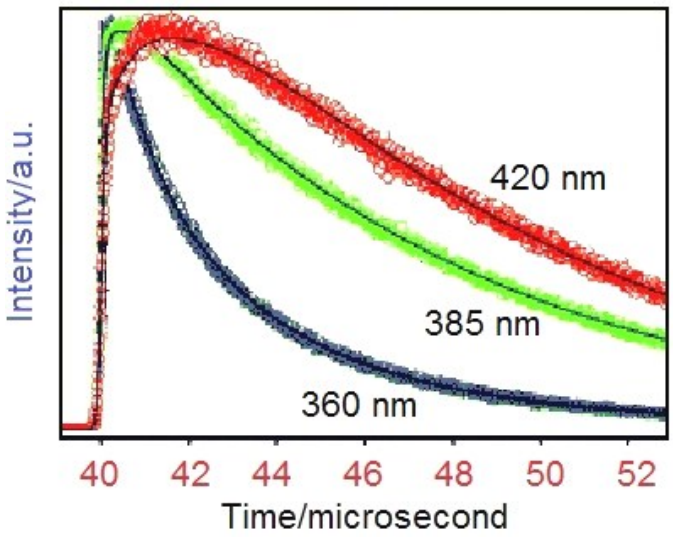

Fig. S11(C). TRES spectra of 2:1:1 Ni/Co/Ti LDH at different excitation wavelengths

The average lifetime of the photo-generated charge carriers of the LDH at 420 nm excitation wavelength 5.68 µs, which is 1.24 and 2.07 times longer than that observed at 360 nm and 385 nm excitation wavelengths. Thus, the photo-excited electrons or holes with a longer life time, generated by photons of wavelength in the visible region, on the LDH surface have been found to be advantageous for the decomposition of the aqueous dyes.

Table S4. Lifetime of photo-generated charges of the LDH at different wavelengths[a]

λ_{ex} (nm)	A_1	τ_1 (µs)	A_2	τ_2 (µs)	τ (µs)
360	7237.3	6.219	3042.3	4.043	2.74
385	5573.4	2.258	4378.1	5.718	4.58
420	6078.6	6.314	4696.7	4.157	5.68

[a] All the data in Table 1 is calculated from TRES analysis of 2:1:1 Ni/Co/Ti LDH

iv) Mechanism of photoluminescence

The mechanism of photoluminescence has been explained on the basis of its results and is schematically illustrated in **Fig. S11(D)** of ESI†. It is observed that the nanomaterial on being excited at 360, 385 and 420 nm respectively above its band gap energy, a part of the energy is being consumed for promoting the electron from the valence band (VB) to the conduction band (CB), leaving holes in the VB, and the remaining part is most likely used to impart kinetic energy to the electron, from where some of them is likely to jump to the conduction band maximum (CB_{max}). From there it is likely to undergo non-radiative transition and hops to the bottom of the conduction band **(Step 1)** further may undergo direct UV emission **(Step 2).** Some of the electrons is are likely to be be trapped by the shallow and deep trap centres and then emit light **(Steps 3 and 4).** From there the electrons are likely to hop to the d-states and further undergo recombination with the holes present in the valence band **(Step 5).** This process however is likely to delay the recombination of the carriers, which is evident from the lifetimes of the carrier species. In this way the LDH nanomaterial, possessing defects and oxygen vacancies assists in the photodegradation of dyestuffs.[5, 11]

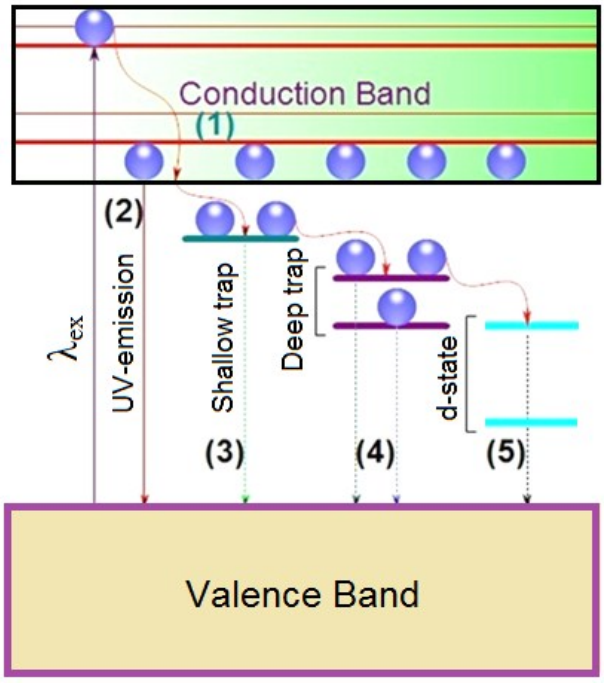

Fig. S11(D). Mechanism of photoluminescence emission

S11. UV-Vis DRS and Zeta potential measurements

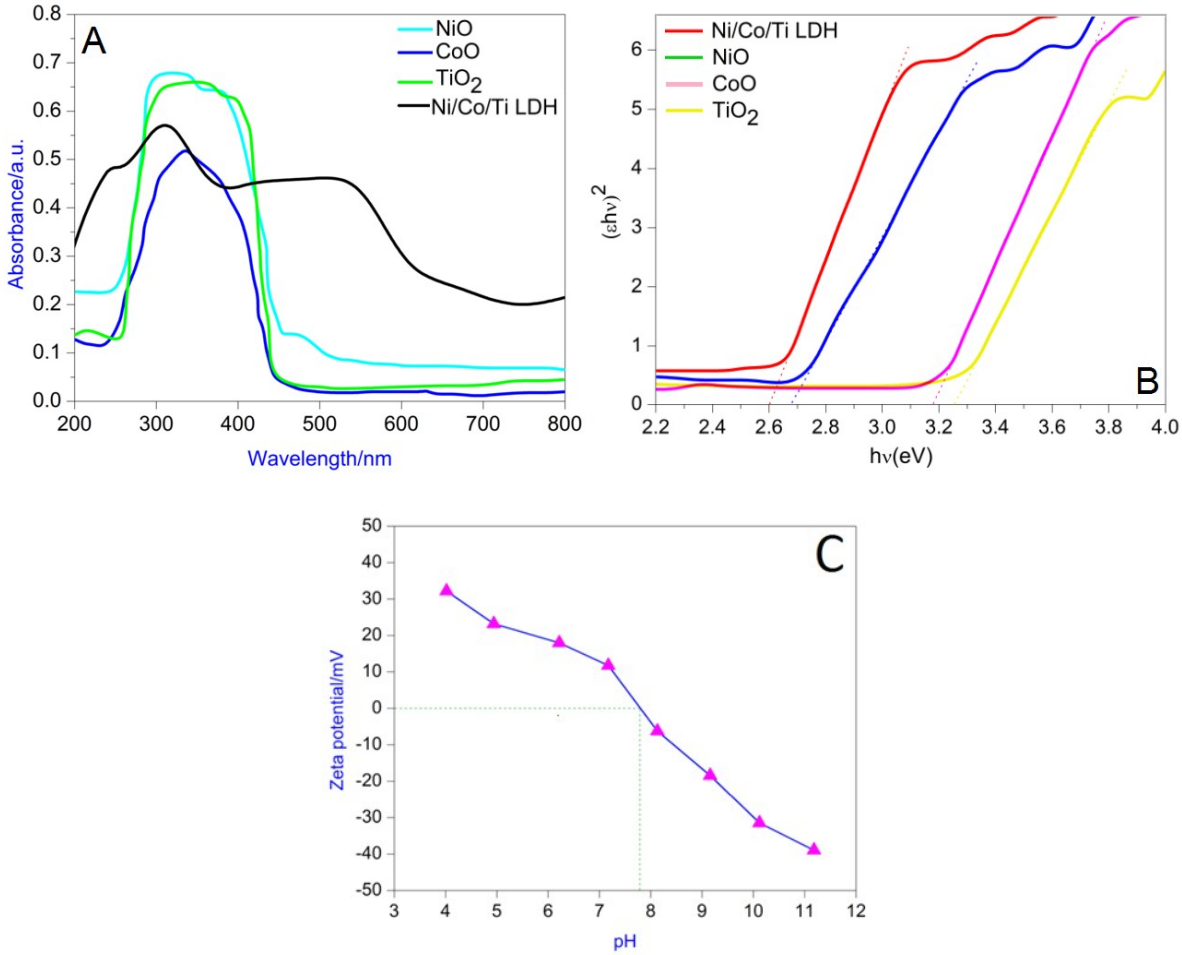

Fig. S12. (A) UV-vis DRS spectra (B) Tauc plots of Ni/Co/Ti LDH with some commercial catalysts (C) Zeta (ξ)- potential curve of Ni/Co/Ti LDH at different pH values

i) UV-Vis DRS analysis

The UV-vis DRS of the LDH investigates the nature and co-ordination state of Ni, Co and Ti within the layered framework. **[Fig. S12 (A); ESI†]** The hump observed at ~230 nm for the LDH could be attributed to the d-d transitions. The strong absorption band in the region of 250-460 nm, which can be assigned to typical metal co-ordinated to the CO_3^{2-} present in the interlayer galleries.[2, 6-10] The broad shoulder observed between 385 extending upto 700 nm indicates the existence of Ti^{4+} in the brucite like sheets.[2] Meanwhile, the broad valley signifies supramolecular guest–guest (hydrogen bonding and van der Waals forces) or guest–host interactions (electrostatic attraction, hydrogen bonding and van der Waals forces). Compared to

the commercial catalysts, a band broadening accompanied by a red shift is observed in case of Ni/Co/Ti LDH, due to the formation of aggregates.

The comparative analysis of the DRS reveals strong absorbance ranging between 250-450 nm amongst all other commercial catalysts used for comparative study **[Fig. S12 (A); ESI†]**. Moreover, the synthesized LDH nanomaterial exhibited stronger absorption between 385-700 nm, which was not observed in any other commercial catalysts. The stronger absorbance in the visible region makes the nanomaterial, a potential candidate for dye degradations than that of the commercially available photocatalysts like NiO, CoO and TiO_2.

ii) Calculation of band gap using Tauc plots

A comparative analysis of the direct band gap **[Fig. S12 (B); ESI†]** is done to have a better understanding into the semiconducting properties of the LDH nanomaterial with that of some important commercial catalysts; using the classical Tauc approach represented by Eqn. (2) -

$$\varepsilon h\upsilon = K\left(h\upsilon - E_g\right)^n \qquad (2)$$

where, E_g represents the optical band gap, hυ is the photon energy, K is a constant and n depends on the nature of the transition. In case of the LDH, the best fit of $(\varepsilon h\upsilon)^2$ versus hυ was obtained for n = 1/2, suggesting a direct allowed transitions to take place across the energy band gap. The extrapolation of hυ at ε = 0 gives absorption edge energies corresponding to E_g = 2.60 eV. This observation of the band transitions for the LDH is in accordance with the photoluminescence observations. The narrow band gap of the LDH [than that of CoO (2.68 eV), NiO (3.18 eV) and TiO_2 (3.26 eV)] imparts better semiconducting properties in comparison to the commercial photocatalysts. Meanwhile, the red shift, observed in the UV-Vis spectra of the LDH could be attributed to its narrow band gap. Thus combining the results of PL, EIS and DRS it is interpreted that electron-hole pairs could be generated by irradiation with long wavelength of visible light. A decrease of band gap for the LDH could be attributed to the localized gap states induced by Ti^{4+}, accompanied by oxygen vacancies within its layered framework of the LDH.

S12. Photocatalytic reactions

The photodegradation experiments were carried out using a specially designed a photocatalytic reactor **[Fig. S13 (A); ESI†]** comprising of a stainless steel chamber fitted with a 300 W tungsten lamp (Philips 38941-1; PS 25, Frost-6100) as the light source, equipped with a wavelength filter (λ > 400 nm) at the bottom. The photocatalytic experiments were performed at 30 °C (room temperature) and the reaction mixtures were taken in a double walled beaker with continuous circulation of running water through the outer jacket ensuring a constant temperature of the reaction mixture. In the degradation experiments, the reactants were vigorously stirred for 30 min in the dark to establish the adsorption/desorption equilibrium between the catalyst and the dyes **[Fig. S13 (B); ESI†]**, followed by visible light exposure. (The adsorption-desorption equilibrium is analysed as follows- The reaction mixtures of both the test dyes were analysed by taking out 5 ml aliquots at every 10 min intervals (during the 30 min interval in dark, with vigorous stirring, prior to visible light irradiation) and thereby analyzing its centrifugate using a UV-visible spectrophotometer.

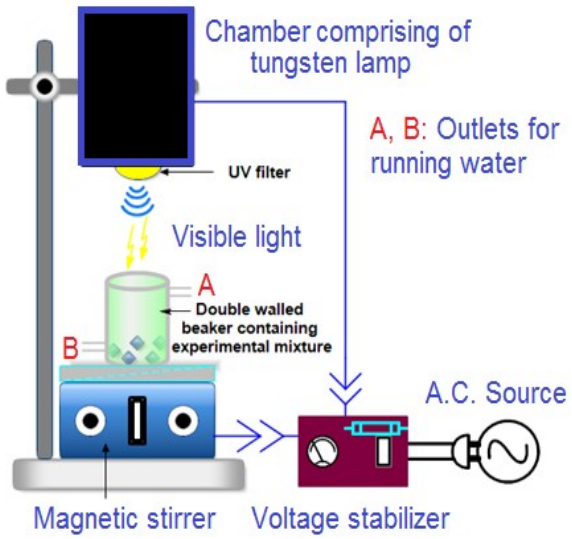

Fig. S13 (A). Schematic of the core section of the visible light photocatalytic device

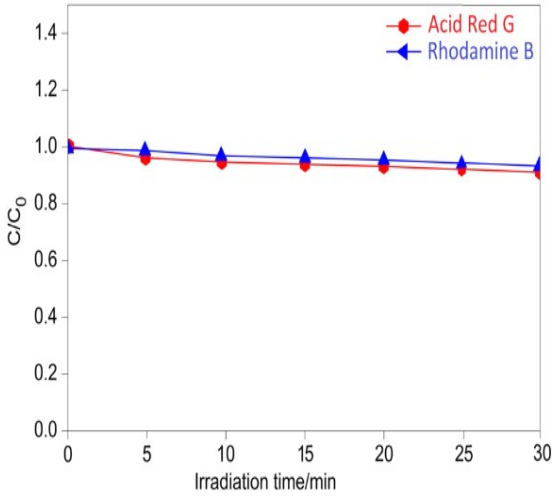

Fig. S13(B). Adsorption-desorption equilibrium between the 2:1:1 Ni/Co/Ti LDH and the test dyes

The plots of C/C_0 Vs irradiation time shows straight lines parallel to X-axis without any change in the C/C_0 values plotted against irradiation time for both ARG and RhB, illustrating the absence of adsorption/degradation during the dark interval prior to the

visible light irradiation. This aspect establishes the fact that adsorption-desorption equilibrium actually takes place between the LDH and the test dyes). At every 10 min intervals, 10 ml aliquots were taken out, centrifuged to remove solid LDH particles and the centrifugate was analyzed for the unconverted dyes using a UV-1800 spectrophotometer at λ_{max} of 530 nm (for ARG) and 553 nm (for RhB) respectively. The decolorization efficiency of the dyes were evaluated using the relationship C/C_0 against time, where C and C_0 represents the absorbance at a particular intervals and at t = 0 min respectively. The decrease in the absorbance values of both the dyes to almost zero upon 60 min of visible light exposure indicated the completion of the decolorization process. In addition, the solution colour changed to nearly transparent thereby marking the end of the decolorization. Blank reactions were carried out following the same procedure without the addition of the catalyst. Control reactions were also performed for both the dyes in the dark for 60 min. The effects of pH on the photocatalytic activities of the test dyes were investigated by variation of the pH of the reaction mixtures from 4.0 to 11.0 by adding either hydrochloric acid or sodium hydroxide (0.1 M). Catalyst loadings of 5.0, 10.0, 15.0 and 20.0 mg in 200 ml dye solutions were used to investigate the effects of the same on RhB photo-degradation at pH 11.0 and for ARG at pH 4.0 at dye concentration of 1.0×10^{-5} M respectively. The photocatalytic conversion of the dyes were also performed with different concentrations of 1.0×10^{-3}, 1.0×10^{-4} and 1.0×10^{-5} M with a LDH loading of 15.0 mg in 200 ml of dye solutions separately under visible light photocatalytic set up. The photocatalytic efficiency of the LDH was compared with that of commercially available pure CoO, NiO and TiO_2 as photocatalyst (15.0 mg in 200 ml of dye solutions) for degradation of both the dyes of concentration 1.0×10^{-5} M. The kinetics of photodegradation of the dyes were also evaluated under optimum conditions (concentration = 1.0×10^{-5} M; catalyst dose= 15.0 mg; pH= 4 for ARG and pH=11 for RhB; 30 °C). The photocatalytic effects were also studied separately with respect to different quenchers like 2Na-EDTA (h^+ scavenger), n-butanol (•OH scavenger), benzoquinone ($O_2^{\bullet -}$ scavenger) at the beginning of the dye degradation experiments in order to establish indirectly the roles played •OH, h^+ and $O_2^{\bullet -}$ species in photodegradation, thereby establishing the semi-conduction mechanism of photocatalysis. The presence of hydroxyl radical (·OH), generated from the LDH during photoassisted degradations was further confirmed by using

a terephthalic acid (TA) fluorescence probe method. The superoxide radicals $(O_2^{\bullet -})$ generated on the LDH during photocatalysis was investigated by electron paramagnetic resonance (EPR) spectroscopy, recorded using a Bruker EMX X-band spectrometer with a field modulation of 100 kHz. The photostability of the synthesized LDH was evaluated by comparative FT-IR analysis of the LDH, with that recovered after the fifth catalytic cycle of degradation. The FT-IR analysis of the colourless end products of both the dyes were compared with the pure dyes to evaluate whether adsorption or degradation dominated the decolorization reactions.

S12.1. Effect of LDH dose

The catalyst dose is an important factor that controls the rate of degradation. This is studied by varying the amount of catalyst concentration between 5.0 mg - 20.0 mg (in 200 ml of the experimental dye solutions having dye concentrations of 1 x 10^{-5} M) and the C/C_0 plots vs irradiation time are shown in **Figs. S14(A)** and **S14(B); (ESI†)** for both ARG and RhB respectively.

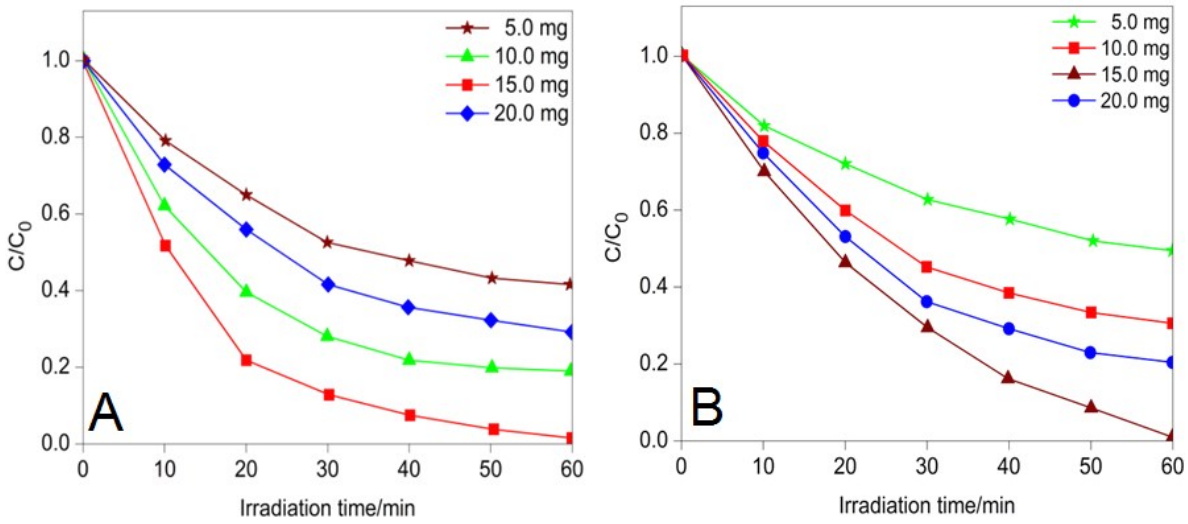

Fig. S14. The effect of catalyst dose on the photodegradation of (A) aqueous ARG [@ pH=4; ARG concentration= 1x10^{-5} M] and (B) aqueous RhB [@ pH=11; RhB concentration= 1x10^{-5} M]

Thus, on increasing the catalyst dose from 5.0 mg to 15.0 mg, the decolorization efficiency was found to increase for both the dyes respectively. It is seen that the LDH could degrade ~99.6 % of ARG and ~99.8 % RhB at 15 mg of catalyst dose, under these

conditions. This have resulted from an increase in the available surface area or the active sites of the catalyst. However, the degradation efficiency decreased with the increase of the catalyst load further to 20.0 mg with both the dyes. Heterogeneous photocatalytic reactions are known to show proportional increase in photodegradation with catalyst loadings.[2, 6] In a given photocatalytic application, the optimum catalyst concentration is to be determined, in order to avoid excess catalyst and ensure total absorption of efficient photons. This is due to the fact that unfavourable light scattering and reduction of light penetration into the solution is occurs with excess photocatalyst loading. So, a decrease in degradation efficiency was observed when the LDH dose was further increased to 20.0 mg. On the basis of this observation the catalyst loading was kept at 15.0 mg in the degradation experiments for obtaining the maximum performance with both the dyes.

S12.2. Effect of pH

The efficiency of decolorization is controlled by pH of the dyes. The pH effects on photoassisted degradations were carried out with both the dyes using 15.0 mg of the LDH; $1x10^{-5}$ M dye solutions within the pH range of 4.0 to 11.0 by addition of drops of either HCl or NaOH (0.1 M). The plots of C/C_0 vs irradiation time for aqueous ARG and RhB are presented in **Fig. S15 (A, B)** of **ESI†**. The ARG dye showed ~ 99.6 % degradation particularly at pH 4. This is due to the fact that the LDH surface possessed positive charge at low pH levels that has resulted in electrostatic interactions between the positively charged surface and the ARG anions in aqueous medium, thereby providing maximum performance. However, at pH values higher than the zero point charge (zpc) of the LDH, the LDH surface attains negative electrostatic charge and are repelled by the ARG anions leading to a decrease in the photocatalytic performance. But a reverse trend is being observed for the cationic RhB dye. In acidic medium, however, the degradation was found to be low because at low pH, as H^+ ion competes with the RhB cations for the available adsorption sites on the LDH surface. Moreover, zeta potential results indicates the positively charged LDH surface at low pH values, which would lead to an electrostatic repulsion with the RhB cations. However, in the alkaline medium, at pH 11, the positively charged LDH molecules electrostatically attract the RhB cations yielding ~ 99.8 % decolorization efficiency.

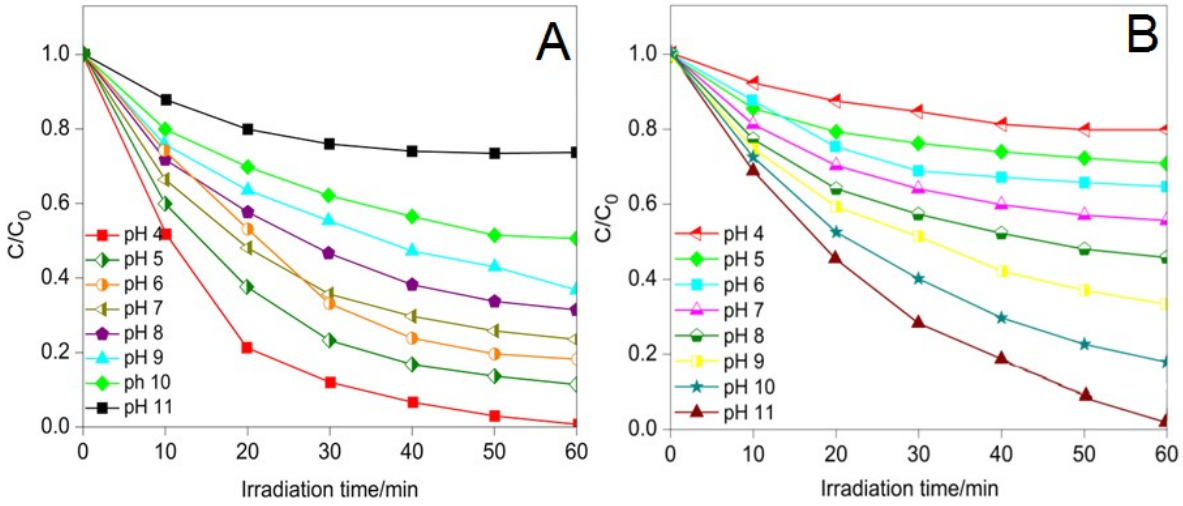

Fig. S15. The effect of catalyst dose on the photodegradation of (A) aqueous ARG and (B) aqueous RhB [@ LDH dose = 15.0 mg; concentration of dyes = $1x10^{-5}$ M]

S12.3. Effect of initial dye concentration

The efficiency of photoassisted decolorization of the cationic and anionic dyes is directly dependant on the initial dye concentration. The photocatalytic effects were observed at optimum pH for the respective dyes (pH 4 for aqueous ARG and pH 11 for aqueous RhB) with 15.0 mg of catalyst dose at 30 °C **[Fig. S16 (A, B); ESI†].** Here, the initial dye concentrations are kept at 1 x 10^{-3}, 1 x 10^{-4} and 1 x 10^{-5} M respectively for both the dyes. Around 99.6% degradation of ARG and 99.8 % degradation for RhB have been achieved with 1 x 10^{-5} M solution of the dyes at room temperature (~30 ^{0}C). Above this concentration, the degradation rate decreased to 81% and 68 % for aqueous ARG and 77% and 54% respectively for aqueous RhB at 1 x 10^{-4} M and 1 x 10^{-3} M dye solutions respectively. The main reason is that when the initial dye concentration is increased, more and more dye molecules get adsorbed on the surface of the LDH. The large amount of adsorbed dye causes an inhibitive effect on the photocatalytic reaction of dye molecules with photogenerated holes, hydroxyl radicals or superoxide radicals because of the lack of any direct contact between them. Moreover, high dye concentration may act as inner filter which shunts the photons away from the LDH surface. Besides this, most of the dye molecules after getting adsorbed on the LDH surface blocks the active surface sites present in the LDH and hence the photodegradation efficiency decreases.[8-11]

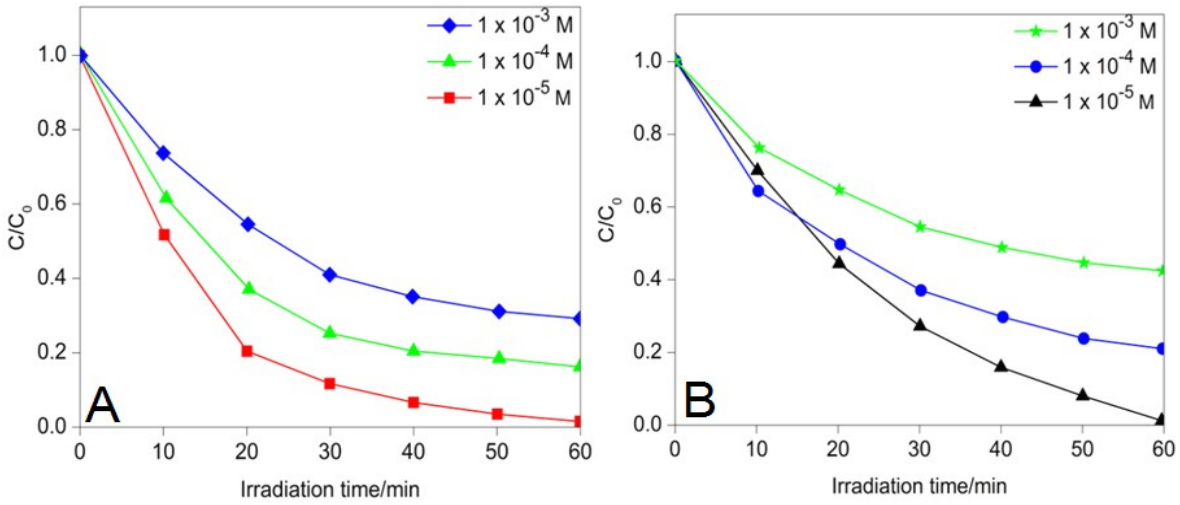

Fig. S16. The effect of initial dye concentration on the photodegradation of (A) Aqueous ARG and (B) Aqueous RhB [@ pH = 4; for ARG and pH = 11 for RhB; catalyst dose = 15.0 mg in 200 ml of aqueous solution of dyes]

S12.4. Recyclability of the LDH

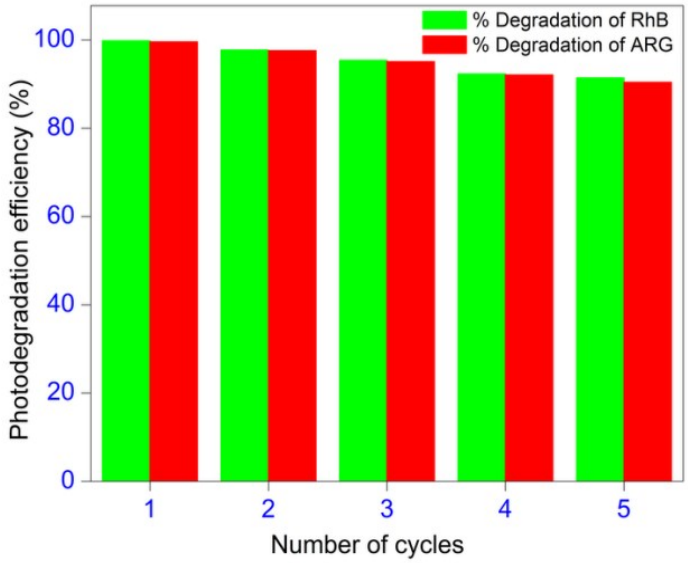

Fig. S17. Number of cycles of RhB and ARG photodegradation over 2:1:1 Ni/Co/Ti LDH

S12.5. Photostability of the LDH

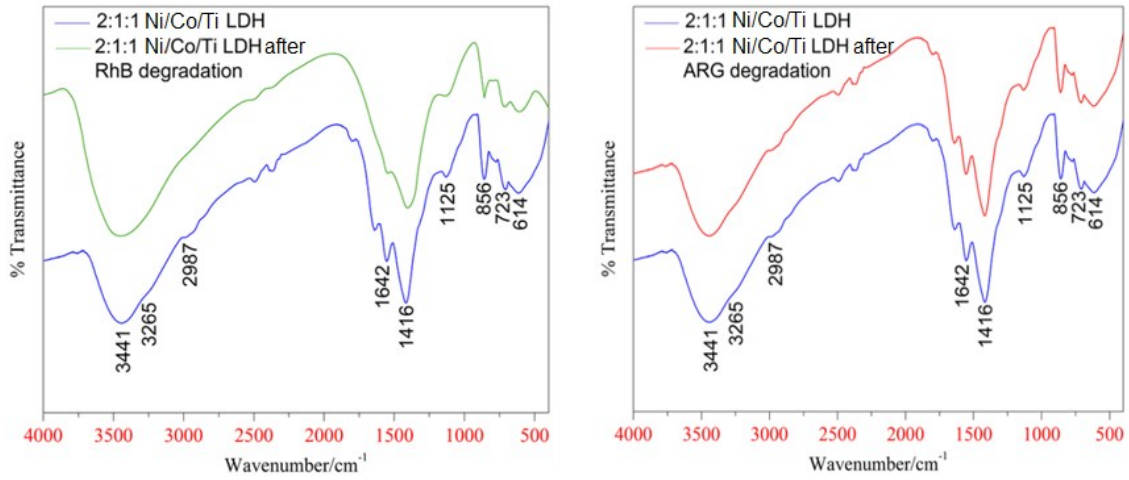

Fig. S18. FT-IR spectra of 2:1:1 Ni/Co/Ti LDH before and after (A) RhB (B) ARG degradations

S12.6. Photoassisted degradation kinetics

The kinetics of photoassisted degradation for both the test dyes was evaluated under optimum conditions (pH = 4 for ARG and pH = 11 for RhB; LDH dose = 15.0 mg; dye concentration=$1x10^{-5}$ M) to understand the degradation characteristics under visible light by the synthesized 2:1:1 Ni/Co/Ti-LDH nanomaterial. The plot of ln (C_0/C) vs irradiation time **[Fig. S19 (A, B); ESI†]** approached very close to linearity indicating that the degradation of both the test dyes by the Ni/Co/Ti LDH photocatalyst follows pseudo first-order kinetic model, which has been represented by the following Langmuir-Hinshelwood Eqn. (3)-

$$\ln\left(\frac{C_o}{C}\right) = k_{app}t \qquad (3)$$

where C_0 is the initial concentration of the dye and C is the concentration at time t. The apparent rate constant k_{app} was calculated to be 0.064 min^{-1} for ARG and 0.041 min^{-1} for RhB. Moreover, the half life was found to be 10.83 min and 16.91 min respectively with ARG and RhB respectively, which has been calculated from k_{app} by using the Eqn. (4)-

$$t_{1/2} = \frac{ln2}{k_{app}} \qquad (4)$$

Thus, the photodegradation kinetics best fitted with the pseudo first order model, which

indicated that the rate of the reaction is primarily dependent on light intensity and absorption efficiency of the catalyst.

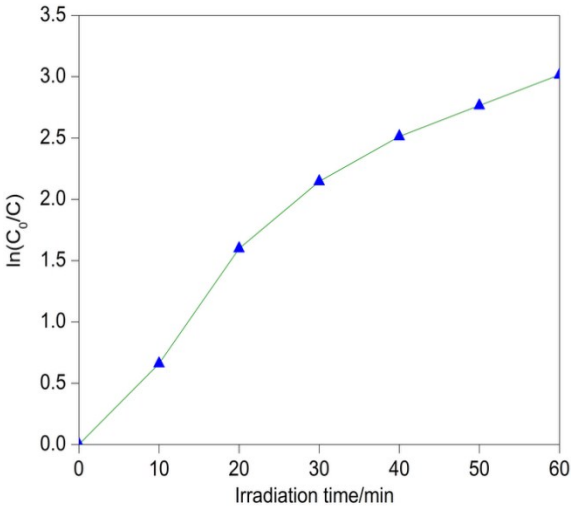

Fig. S19(A). Plot of $\ln(C_0/C)$ vs time for 2:1:1 Ni/Co/Ti LDH [@ pH=4; catalyst dose=15.0 mg in 200 ml of aqueous ARG of $1x10^{-5}$ M]

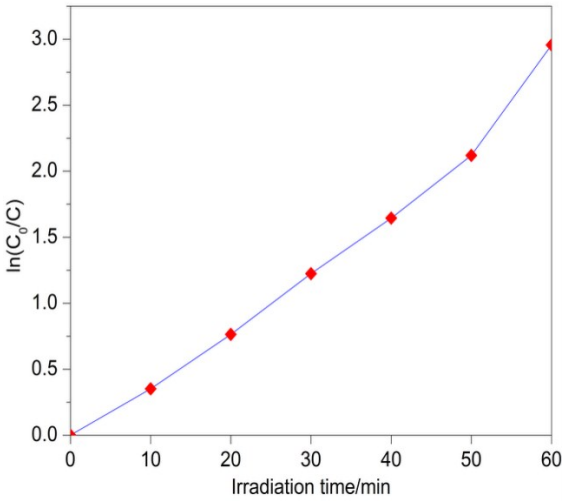

Fig. S19(B). Plot of $\ln(C_0/C)$ vs time for 2:1:1 Ni/Co/Ti LDH [@ pH=11; catalyst dose=15.0 mg in 200 ml of aqueous RhB of $1x10^{-5}$ M]

3.12.7. Roles played by quenchers on photodegradation

The photocatalytic reactions of the semiconductors are driven mainly by active species like $^{\bullet}OH$, h^+ and $O_2^{\bullet-}$. The presence of $^{\bullet}OH$, generated from the 2:1:1 Ni/Co/Ti LDH during photoassisted degradations was measured using a terephthalic acid (TA) fluorescence probe method. The procedure of detection of $^{\bullet}OH$ is similar to that of photocatalysis except that 1 x 10^{-5} M TA in 4 x 10^{-5} M NaOH solution replaced the dye solutions during the photocatalysis with the LDH. TA undergoes reaction with $^{\bullet}OH$ producing a highly fluorescent compound- 2-hydroxyterephthalic acid, which shows PL emission peak at 426 nm on being excited with light of 315 nm wavelength **[Fig. S20(A); ESI†].** The PL spectrum was analysed on a Hitachi F-2500 FL spectrophotometer. However, no PL signal was observed for the same experiments performed in the absence of visible light irradiation, indicating the generation of $^{\bullet}OH$ radical by the LDH under visible light. Moreover, the surface -OH groups present on the LDH could easily form the $^{\bullet}OH$ radicals that controls the photocatalytic reactions.[7]

The presence of $^{\bullet}OH$ radicals was further confirmed by external addition of n-butanol,

(a quencher of •OH) prior to the photocatalytic experiments under the same set of experimental conditions.[8] It is seen that the rate of photodegradation of both the dyes were suppressed to a considerable extent, indicating that •OH is one of the active species that controls the rate of photodegradation **[Fig. S20 (C); ESI†]**.

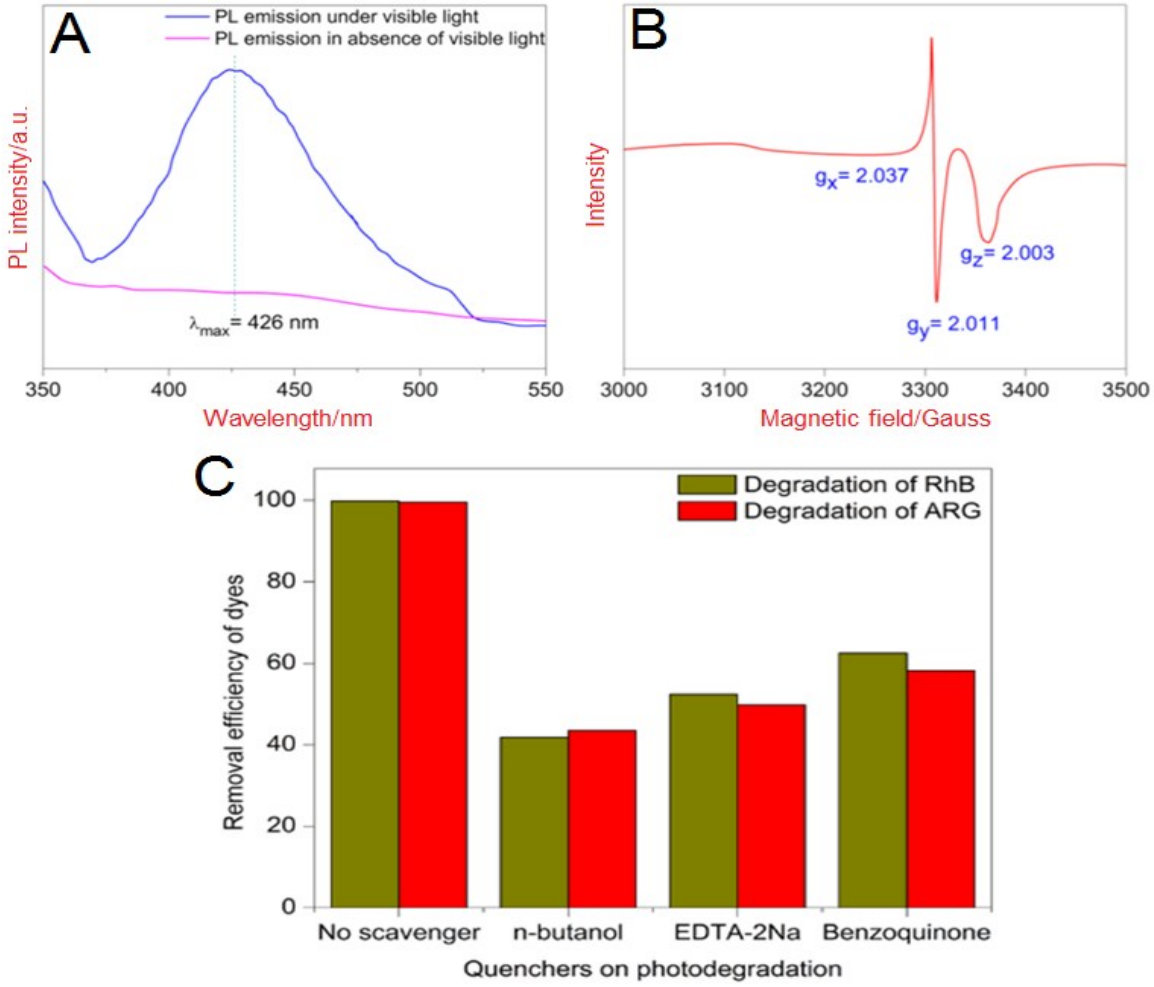

Fig. S20. (A) PL spectral changes with visible-light irradiation over the Ni/Co/Ti LDH in basic solution of terephthalic acid (TA) for detection of •OH radicals (B) EPR spectrum of the LDH for detection of $(O_2^{\bullet -})$ species (C) Effect of quenchers on photodegradation of RhB and ARG by Ni/Co/Ti LDH

On the other hand the superoxide $(O_2^{\bullet -})$ species generated by the Ni/Co/Ti LDH during photocatalysis was investigated by electron paramagnetic resonance (EPR) spectroscopy, recorded using a Bruker EMX X-band spectrometer with a field modulation of 100 kHz.

The frequency calibration was performed using a frequency counter microwave bridge (ER 041 XG-D). In the EPR analysis, DPPH was used as field marker (g = 2.0036). The HPA 400/30S lamp (400 W, Philips) was used as the irradiating light source for EPR analysis. The magnetic field values of the radical was determined using the formula $h\nu = g\beta H$. Prior to the analysis, the synthesized LDH was subjected to thermal treatment at 473 K in vacuum followed by exposure to an oxygen environment at room temperature. The EPR spectrum of the LDH **[Fig. S20 (B); ESI†]** analysed under O_2 environment under visible light ($\lambda > 400$ nm) showed signals at $g_x = 2.0037$, $g_y = 2.011$ and $g_z = 2.003$, which coincides with the g-tensor of the $O_2^{\bullet -}$ species. Therefore the presence of superoxide leads to the generation of visible light-sensitive redox centers responsible for the degradation of the dyes.

The indirect radical trapping experiments was also performed with both the dyes by external addition of benzoquinone (BQ) ($O_2^{\bullet -}$ scavenger), which resulted in the decrease of photocatalytic performance of the LDH,[8] thereby confirming the presence of superoxide as the active species during degradations **[Fig. S20 (C); ESI†]**.

Moreover, the observed degradation of both aqueous ARG and RhB were further suppressed by the external addition of ethylenediaminetetraacetate (h^+ scavenger) prior to the photocatalytic experiments, indicating that h^+ were also the important species generated on the LDH surface by visible light irradiation, which also contributed to the degradation of dyestuffs.[8]

S12.8. FT-IR analysis of the end products of photodegradation

The occurrence of adsorption or degradation in the decolorization of both ARG and RhB in aqueous media is determined by the comparative FT-IR analysis of the end products (taken after centrifugation of the of the dark reaction, blank reaction and at the end of the photocatalytic reactions with the LDH) were co-related with that of pure dyes **[Figs. S21(A, B); ESI†]**. The comparative analysis of the FT-IR spectra reveals the presence of all the characteristic bands at their respective positions for the control experiments with the dyes (blank and dark reactions). However, some of the peaks became broad in the fingerprint regions, indicating that adsorption dominated the control experiments of both the dyes with

the synthesized LDH. Further, the FT-IR spectra of the decolorized end products after 60 min reveals the absence of most of characteristic bands of both the dyes accompanied by the emergence of peaks in new positions, signifies that the complex dye has been degraded to simple smaller molecules marking the end of the photocatalytic reactions.

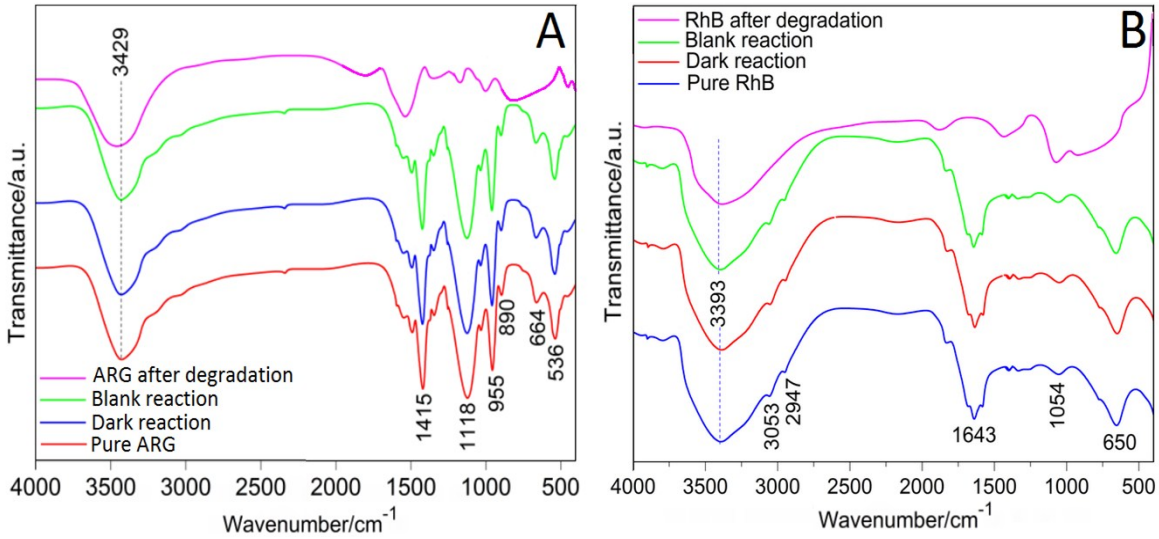

Fig. S21 (A, B). Comparative FT-IR analysis of the pure dyes, control experiments and the photodegradation products.

S12.9. Proposed mechanistic pathways of photodegradation

On the basis of the results of the XPS, PL, EIS, DRS, TA fluorescence probe, EPR and indirect radical and hole trapping analyses, the mechanistic pathways of the photoassisted degradations of the test dyes by Ni/Co/Ti LDH has been illustrated in the light of band theory, taking O1s orbital as the Ni2p, Co2p and Ti2p energy levels as the conduction band. The photocatalytic degradation is supposed to take place in two different pathways by the generation of reactive species like •OH and $O_2^{\bullet-}$ in presence of visible light.

First pathway: A series of reactions is supposed to take place in the following sequential pattern **(Eqs. 5 to 17)** upon visible light exposure at 30 °C. The electrons are first excited from valence band to conduction band, thereby leaving holes in the valence band. The absorption of photons initiates electronic excitation with energy equal to or greater than the band gap energy of the semiconductor LDH nanomaterial. Thus, 2:1:1 Ni/Co/Ti LDH generates e^--h^+ pairs **(Eq. 5)** upon visible light exposure, thereby reducing Ni^{2+}, Co^{3+}

and Ti^{4+} species on the LDH surface **(Eqs. 6-8).** A strong redox reaction is generated **(Eq. 9)** which is initiated by the photo-generated electrons with intense lattice vibrations on the LDH surface. The h^+ hops within the LDH surface and reacts with H_2O and OH^- ions yielding OH• radicals **(Eqs. 10, 11).** The e^- are likely to react with adsorbed oxygen species producing superoxide ($O_2^{\bullet -}$) radicals **(Eq. 12).** Superoxide ($O_2^{\bullet -}$) species further undergoes further transformation with the adsorbed H^+ present on the LDH surface to producing peroxide radicals (•OOH) **(Eq. 13),** further yielding H_2O_2 **(Eq. 14)** as well as hydroxyl radicals (•OH) **(Eq. 15).** Hydroxyl (•OH) and superoxide ($O_2^{\bullet -}$) radicals are very highly reactive species that mineralize the dye to simple molecules **(Eq. 16).** This follows the recombination between the h^+ and e^- with the dissipation of energy and reduction of quantum efficiency **(Eq. 17).** The pathway involves the sequence of reactions as follows:-

$$Ni/Co/Ti\ LDH + h\upsilon \longrightarrow Ni/Co/Ti\ LDH\ \left(e^- + h^+\right) \quad (5)$$

$$Ni^{2+} + 2e^- \longrightarrow Ni^0 \quad (Electron\ trap) \quad (6)$$

$$Co^{3+} + e^- \longrightarrow Co^{2+} \quad (Electron\ trap) \quad (7)$$

$$Ti^{4+} + e^- \longrightarrow Ti^{3+} \quad (Electron\ trap) \quad (8)$$

$$Ni^{2+} + Co^{3+} + Ti^{4+} + 4e^- + h\upsilon \leftrightarrow Ni^0 + Co^{2+} + Ti^{3+} \quad (Migration) \quad (9)$$

$$h^+ + H_2O \longrightarrow HO^\bullet + H^+ \quad (10)$$

$$h^+ + OH^- \longrightarrow HO^\bullet \quad (11)$$

$$O_2 + e^- \longrightarrow O_2^{\bullet -} \quad (12)$$

$$O_2^{\bullet -} + H^+ \longrightarrow HOO^\bullet \quad (13)$$

$$HOO^\bullet + HOO^\bullet \longrightarrow H_2O_2 + O_2 \quad (14)$$

$$H_2O_2 + O_2^{\bullet -} \longrightarrow HO^\bullet + OH^- + O_2 \quad (15)$$

$$Dyes + O_2^{\bullet -} + HO^\bullet \longrightarrow Degradation\ products \quad (16)$$

$$h^+ + e^- \longrightarrow Energy \quad (17)$$

Second pathway: The second pathway proceeds through the photosensitization of the dyes in presence of visible light.[8-10] In this process, the dye molecules act as a sensitizer by

the absorption of visible light to yield an excited state of the sensitizer **(Eq. 18)**, further transforms to dye radicals with the release of electrons **(Eq. 19)**. The dye radicals thus generated forms intermediate products like CO_2 and H_2O **(Eq. 20).** These electrons are injected into the conduction band of the LDH photocatalyst **(Eq. 21)** where it is scavenged by O_2 to form $O_2^{\bullet -}$ species as shown in **(Eq. 2)** further yielding H_2O_2 **(Eq. 23).** The electron transfer from the excited dye molecule to the conduction band of LDH usually is too fast (in the range of tens of femtoseconds). Further H_2O_2 subsequently generates •OH radicals (Eq. 24). The •OH radicals further degrades the complex dye to simple molecules (Eq. 25). The formed species photodegrade the dye molecules as follows:

$$Dye + h\upsilon \longrightarrow Dye^{*} \quad (18)$$

$$Dye^{*} \longrightarrow Dye^{\bullet +} + e^{-} \quad (19)$$

$$Dye^{\bullet +} \longrightarrow CO_2 + H_2O \quad (20)$$

$$Ni/Co/Ti\ LDH + e^{-} \longrightarrow Ni/Co/Ti\ LDH^{\bullet +} \quad (21)$$

$$Ni/Co/TiLDH^{\bullet +} + O_2 \longrightarrow Ni/Co/TiLDH + O_2^{\bullet -} \quad (22)$$

$$O_2^{\bullet -} + 2H_2O + e^{-} \longrightarrow 2H_2O_2 \quad (23)$$

$$H_2O_2 + e^{-} \longrightarrow {}^{\bullet}OH + OH^{-} \quad (24)$$

$$^{\bullet}OH + Dyes \longrightarrow Degradation\ products \quad (25)$$

This observation clearly demonstrate the involvement of holes (h^+), hydroxyl (•OH) and superoxide ($O_2^{\bullet -}$) species as highly reactive agents in the LDH mediated aqueous phase photocatalytic degradation of the cationic Rhodamine B (RhB) and the anionic Acid Red G (ARG) dye.

The XPS and PL measurements suggest the presence of multiple valency of Ni, Co and Ti accompanied by oxygen vacancies in the LDH. The presence of defects and $O_2/O_2^{\bullet -}$ transformation in the LDH has also been confirmed by EIS and EPR analyses. The presence of hydroxyl (•OH) radical is also confirmed by terephthalic acid (TA) fluorescence probe method. The presence of holes (h^+), hydroxyl (•OH) and superoxide ($O_2^{\bullet -}$) species are confirmed by indirect radical and hole trapping experiments, by addition of appropriate

quenchers at the beginning of the photocatalytic experiments of the LDH with both the dyes. On the basis of these data, the mechanistic pathways has been presented in the form of e^--h^+ hopping conduction model and through photosensitization of the dyes. The schematic illustrations of the mechanistic pathways of photodegradation are represented in **Fig. 2 (Pathway 1 and Pathway 2)** of the main article.

S.12.10. GC-MS analysis and elucidation of reaction mechanism of photodegradations

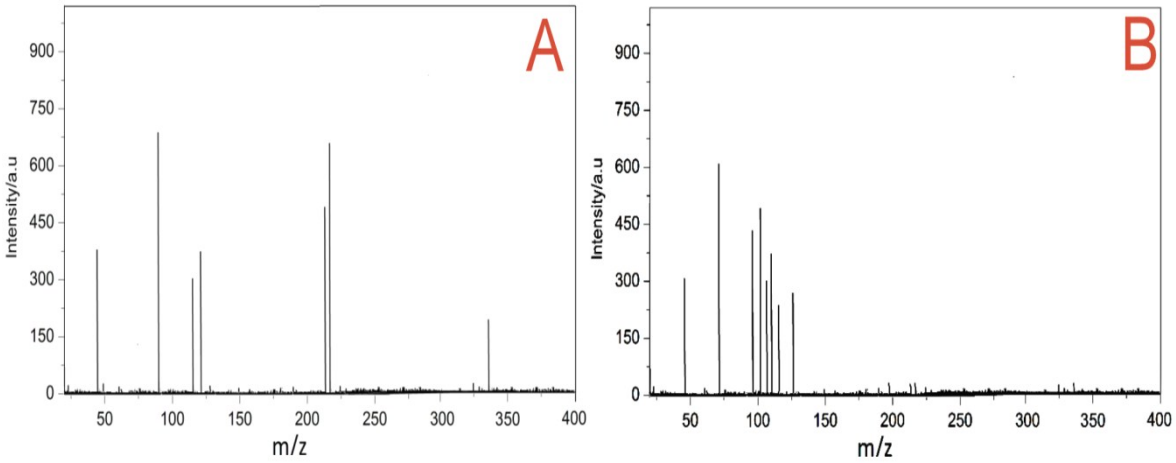

Fig. S22. Mass spectrum of the degradation products of (A) RhB and (B) ARG

Characterization of the final products of photodegradation was helpful in the elucidation of reaction mechanism of dye decolourizations. In this work, GC-MS was employed to obtain an insight into the dye degradation products. The degradation products were collected after the decolorization efficiency reached the maximum (reaction time 60 min, 2:1:1 Ni/Co/Ti LDH = 15.0 mg and dye concentration = 1 x 10^{-5} M). The samples were extracted with dichloromethane. 1µL of the extracted product mixture was injected into the GC-MS. The MS analysis was performed in positive-ion mode. It is evident that the photocatalytic degradation with LDH generates •OH radicals and $O_2^{\bullet -}$ species on vigorous stirring that catalyse the degradation of the dyes in aqueous medium.

Eight products were identified in the mass spectrum of Rhodamine B (RhB) **[Fig. S22 (A); ESI†]** since the complex dye has a diazo structure. The analysis of the mass spectra of the degradation products of RhB suggests that the mechanistic pathway of degradation

proceeds with the asymmetric cleavage of the dye **[Fig. S23(A); ESI†],** which is likely to undergo transformations in three possible pathways. In the first pathway it is suggested that the dye could be broken down to benzoic acid (m/z = 122.02). The second pathway is likely to proceed by the formation of the breakdown products to be N, N-diethyl-acetamide (m/z = 115.08), [4-(2-carboxyphenyl)-2-methylchromen-7-ylidene]-diethylammonium ion (m/z = 336.18) and diethyl-(2-methylchromen-7-ylidene)-ammonium ion (m/z = 216.13).

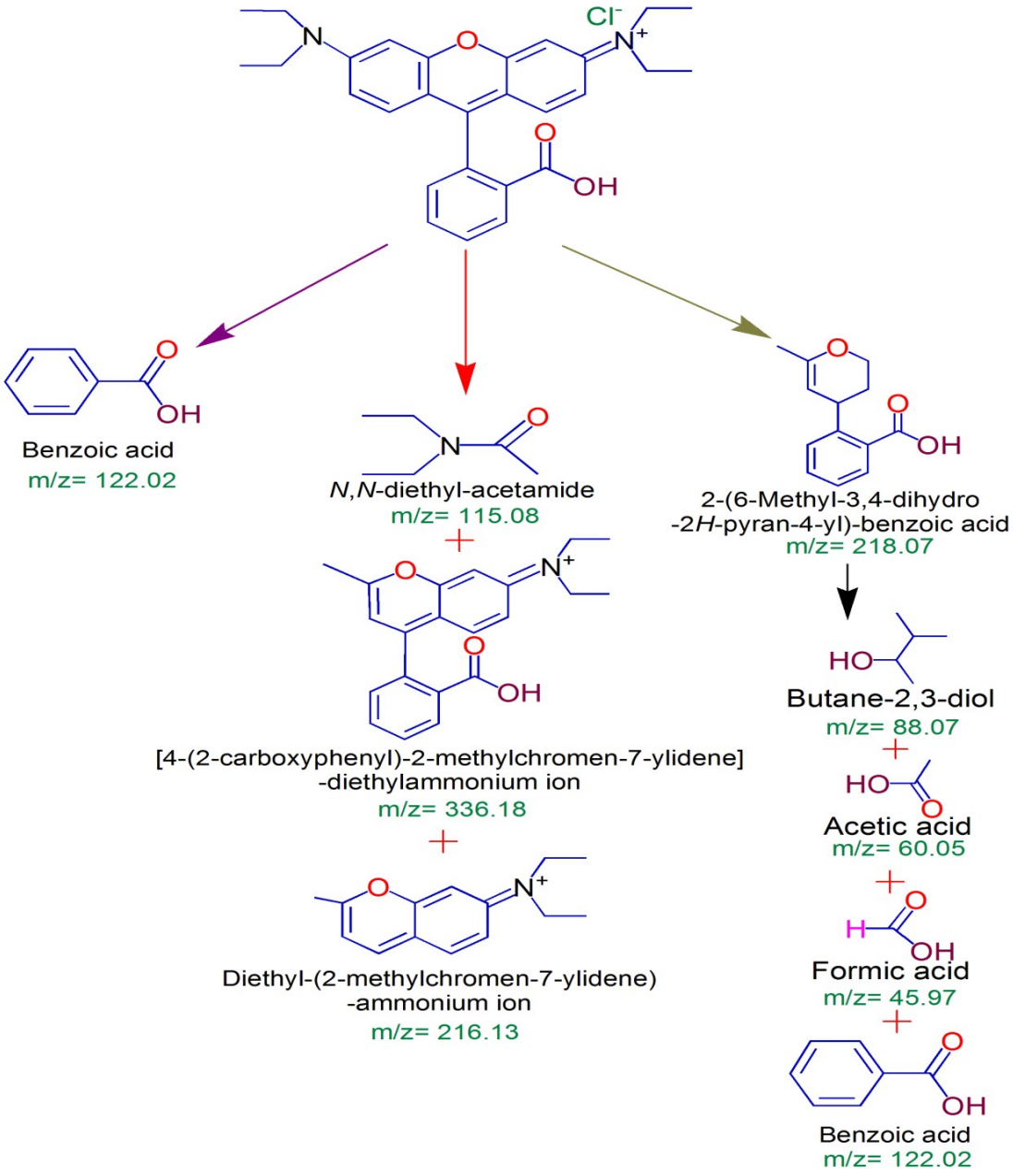

Fig.S23 (A). Proposed reaction mechanism of degradation of aqueous Rhodamine B

The third pathway has been proposed to take place by the formation of 2-(6-methyl-3,4-dihydro-2H-pyran-4-yl)-benzoic acid (m/z = 218.07), which further breaks down to form butane-2,3-diol (m/z = 88.07), acetic acid (m/z = 60.05), formic acid (m/z =45.97) and benzoic acid (m/z = 122.02). The identification of these breakdown products in the mass spectrum of the RhB degraded components supports the asymmetric cleavage mechanism of the dye, thereby suggesting the remarkable photodegradation ability of the LDH.

On the other hand the degradation of the anionic dye Acid Red G (ARG) reveals nine peaks in the mass spectrum of its degraded component. The analysis of the mass spectrum indicates that the anionic dye is likely to undergo transformation to form 1-amino-naphthalene-2,3,6-triol (m/z = 191.2), which further dissociates to form 3-amino-benzene-1,2-diol (m/z = 125.2). 3-amino-benzene-1,2-diol is further broken down to form benzene-1,2-diol (m/z = 110.2), which further yields 1,2-benzoquinone (m/z = 108.8). 1,2-benzoquinone undergoes ring opening to form but-2-ene-dioic acid (m/z = 116.2). It further transforms to form oxalic acid (m/z = 90.01) and acrylic acid (m/z = 71.2). Oxalic acid further undergoes transformation to form formic acid (m/z = 46.01) whereas acrylic acid is transformed to malonic acid having m/z = 103.7. The mass spectra supports this pathway of degradation of of the dye.

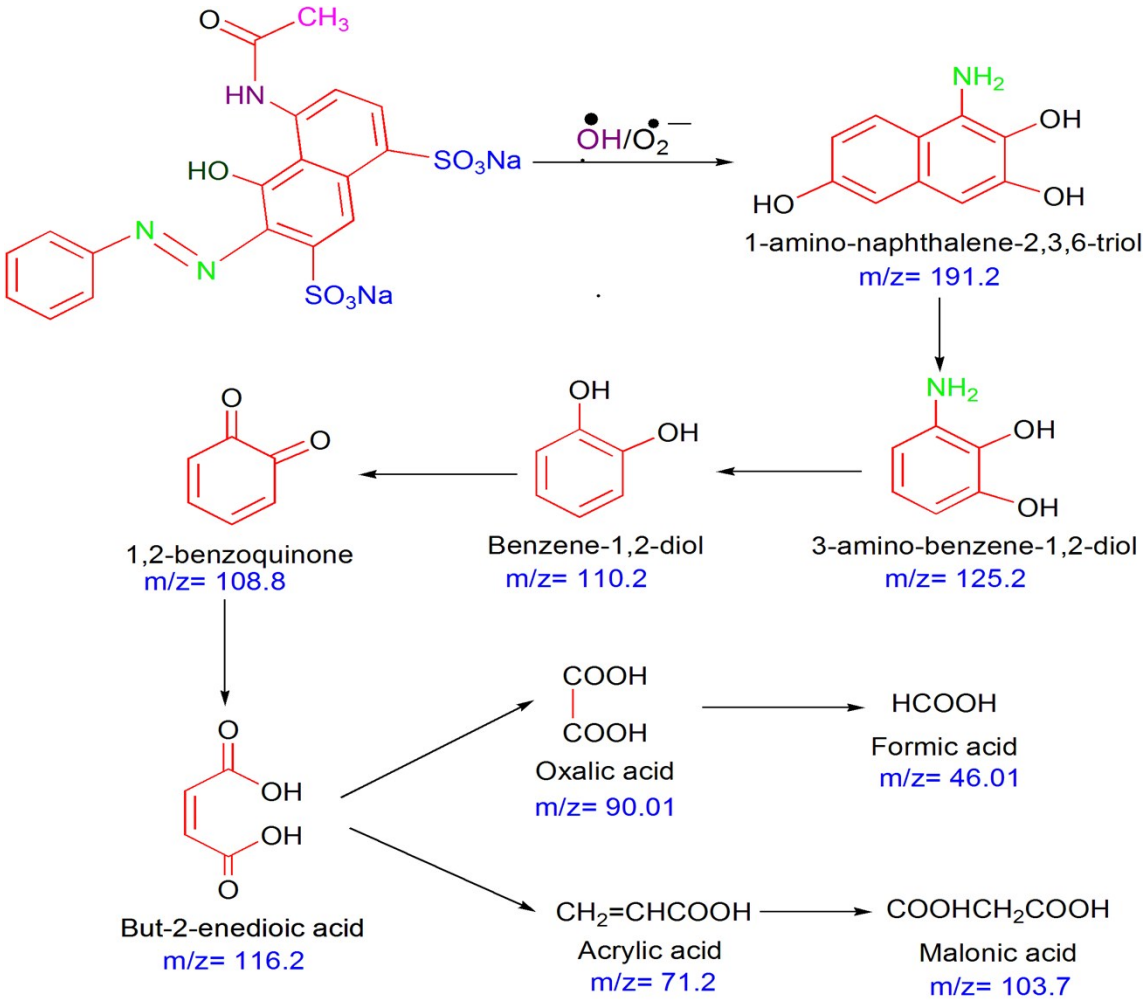

Fig.S23 (B). Proposed reaction mechanism of degradation of aqueous Acid Red G

Thus, from the indirect hole trapping, TA fluorescence probe, EPR and EIS analyses, it is obvious that h^+, $^{\bullet}OH$ and $O_2^{\bullet-}$ were the important active species that contributes to the photodegradation of both cationic as well as anionic dye molecules in aqueous phase to simple and less toxic components than their parent analogues.

S.12.11. Mineralization studies

The final products from the oxidation of dyes are some intermediates, CO_2 and H_2O. The intermediates are most likely to be aromatic compounds which has accounted for the TOC of the solution. Various aromatic compounds are formed during degradations, so, the spectroscopic measurements of dye concentrations does not guarantee the complete mineralization of dye as it only gives the complete or partial reduction in its color. The

process of mineralization involves the complete oxidation of dyes to CO_2 and H_2O. Hence, to observe the complete mineralization of dye, TOC was measured. The percentage reduction in TOC with respect to time for the degraded dye solutions, treated by visible light was evaluated and represented in **(Fig. S24; ESI†)**.

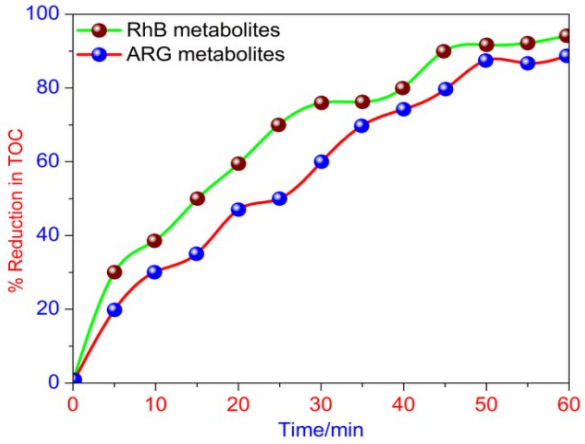

Fig. S24. Percentage reduction in TOC as a function of time at different optimized conditions (volume of solution: 200 ml, initial dye concentration: 1 x 10^{-5} M; pH: 11.0 for RhB and 4 for ARG)

It was found that TOC reduced by 94 % (for RhB metabolites) and (88 % for ARG metabolites) of the original when the degradation was carried out under visible light. Almost 100% decolorization is achieved within 60 min, whereas 94 % and 88 % reduction in TOC was observed for RhB and ARG solutions after 60 min through photocatalysis by the LDH. Thus it could be inferred that the TOC removal rate was less than that of the decolorization process under the same experimental conditions due to the formation of some stable intermediates, as identified using GC-MS studies. However, a higher reduction in TOC for both the dye metabolites infers that the dyes have been degraded to simple molecules than their parent analogues.[11]

S12.12. Closure of Carbon mass balance

Carbon mass balance closure is a unique technique for assessing the accuracy of the measurements. As a result of the carbon mass balance closure, a consistency and accuracy of the internal data is maintained. If carbon mass balance closures approach near 100 %,

then the stoichiometric accuracy of the carbon related processes is considered to be very reliable.

In order to investigate the closure of carbon mass balance, small ports were configured within the reactor top for the purpose of input and removal of water during experimentation. This is accompanied by a port to facilitate the exhaust exit. Influents and effluents aliquots were collected at every 5 min intervals. The analytical instrumentation, was operated under appropriate specifications to quantify the constituents within the photocatalytic system- (a) GC with FID (b) Ion chromatograph and (c) TOC analyser. The inlet and outlet components have been monitored throughout the experiments for determination of the overall mass balance. The exhausts and TOC concentrations were converted to cumulative moles of carbon in each compound and the medium. Inlet carbon contents of the dyes were compared with the accumulated carbon in the reactor and the existing carbon in the exhaust for generation of the overall mass balance for the system. The concentrations of Cl^- have been observed to be below the accurate range of the ion chromatographs and negligible in comparison to the other components, and so the results of chloride ions were not reported.

It is seen that the inlet and outlet moles of carbon were nearly equal at the initial stages of experimentation; however the accumulated and effluent carbon fall to approximately 92 % for RhB system and 90 % for ARG system in comparison to the estimated inlet carbon content. The quantification measurements of the dyes does not indicate any presence of the parent dye content in the inlet gas, exhaust or reactor liquid. Thus with a closure of carbon mass balance, it is very much reasonable to arrive at the conclusion that parent dyes have been mineralized through a relatively rapid pathway.

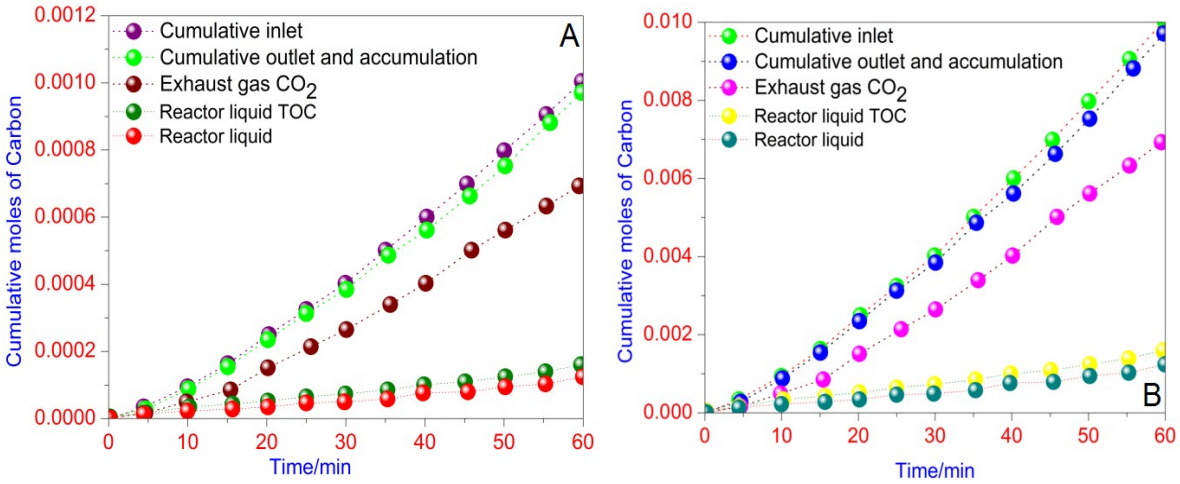

Fig. S25 (A, B). Cumulative moles of carbon in separate forms and media of the system for the degradation of (A) Rhodamine B and (B) Acid Red G.

Supplementary References

1. L. Zou, X. Xiang, M. Wei, F. Li and D.G. Evans, *Inorg. Chem.,* 2008, **47**, 1361.
2. J. He, M. Wei, B. Li, Y. Kang, D.G. Evans and X. Duan, *Preparation of layered double hydroxides, Struct. Bond.*, Springer-Verlag (Berlin), 2006, **119**, 89.
3. M. Shao, J. Han, M. Wei, D.G. Evans and X. Duan, *Chem. Engg. J.,* 2011, **168**, 519.

4. L.W. Zhang, H.B. Fu and Y.F. Zhu, *Adv. Funct. Mater.*, 2008, **18**, 2180.
5. F. Li, L. Zhang, D.G. Evans and X. Duan, *Colloids and Surfaces A: Physicochem. Engg. Aspects*, 2004, **244**, 169.
6. L. Mohapatra and K. M. Parida, *Phys. Chem. Chem. Phys.,* 2014, **16**, 16985.
7. G. Wang, Y. Li, B. Jiang, K. Pan, N. Fan, Q. Feng, Y. Chen and C. Tian, *Chem. Commun.,* 2011, **47**, 8019.
8. M.Q. Yang, N. Zhang, M. Pagliaro and Y.J. Xu, *Chem. Soc. Rev.,* 2014, **43**, 8240.
9. Y. Zhang, Z.R. Tang, X. Fu, and Y.J. Xu, *ACS Nano,* 2010, **4,** 7303.
10. S. Liu, Z.R. Tang, Y. Sun, J.C. Colmenares and Y.J. Xu, *Chem. Soc. Rev.,* 2015, **44**, 5053.
11. P. Roy Chowdhury and K.G. Bhattacharyya, *Dalton Trans.*, 2015, **44** 6809.